EVOLUTION OF BINARY SYSTEMS EMBEDDED IN CIRCUMBINARY ACCRETION DISKS

by

Justin Ross Bankert

A dissertation submitted to The Johns Hopkins University in conformity with the requirements for the degree of Doctor of Philosophy.

Baltimore, Maryland

August, 2017

Abstract

In this work, I combine two studies on circumbinary accretion disks. The first study focuses on the interactions between a central equal mass binary and a surrounding retrograde circumbinary accretion disk. The second study examines the evolution of the orbital parameters (semi-major axis a and eccentricity e) of a binary on an eccentric orbit embedded in a prograde circumbinary accretion disk. In both studies, we utilize three-dimensional, MHD simulations.

In the first study, we find that the binary-on-disk torque is much smaller for a retrograde circumbinary disk than for a disk orbiting in the prograde direction. Thus, fluid in a retrograde circumbinary disk can accrete directly from the disk to the binary's domain. There is no "gap" carved out of the retrograde disk. Also, retrograde disks do not develop the large-amplitude lumps generically seen near the inner edges of prograde disks. Because the disks angular momentum is directed oppositely to that of the binary, accretion onto the binary causes a rapid increase in eccentricity. Lastly, we discuss the comparative rates of orbital evolution associated with accretion in prograde and retrograde circumbinary disks, finding that the principal contrast is that $\dot{e}$ should be rather greater in the retrograde case.

In the second study, we find that for prograde circumbinary accretion disks around binaries on eccentric orbits, as was found for the case of circular binaries, accretion occurs through transient accretion streams, which traverse the gap region between the binary and the bulk disk. However, the $m = 1$ "lump" feature found in the circular case did not develop in any of the eccentric binary cases. Instead, we found prominent $m = 2$ spiral density waves in the bulk disk. We observed a monotonic increase in the

time averaged mass accretion rate with increasing binary orbital eccentricity. The rate of mass accretion peaks during the binary descent phase, although this trend is weaker for larger eccentricities. Even so, accretion into the binary region occurs primarily near apoapsis for all binary orbital eccentricities. As the binary nears apoapsis, negative binary-on-disk torques extract angular momentum from accretion streams allowing material to cross the gap and pass into the binary region. Postive binary-on-disk torques propel accretion streams back into the gap region a short time (less than a binary orbit) later. This effect is more pronounced for small eccentricity binaries; smaller eccentricity binaries thus have larger populations of disk material with a high ratio of $\left|\frac{v_r}{v_\phi}\right|$. We find that, on average, prograde circumbinary accretion disks increase (or at least do not decrease) the net angular momentum of the central binary. Utilizing simple ballistic calculations, we find that the majority of material passing into the binary region does not impact a binary mini-disks within a binary orbital time for $e \gtrsim 0.3$. We conclude that future work must contain the binary region on the computational grid in order to accurately model the binary evolution.

Thesis Advisor	Professor Julian H. Krolik	The Johns Hopkins University
Committee Member	Professor Ethan Vishniac	The Johns Hopkins University
Committee Member	Professor Oleg Tchernyshyov	The Johns Hopkins University
Committee Member	Professor Thomas Haine	The Johns Hopkins University
Committee Member	Doctor Steve Lubow	Space Telescope Science Institute

Acknowledgments

First and foremost, I would like to thank my parents for instilling in me a strong desire to learn. They always encouraged me to push myself academically. I would most certainly not be where I am today without their guidance and support. Even from a young age, my mother insisted that I would one day go to college. This may not seem especially noteworthy, except for the fact that neither of my parents attended college, nor did any of their parents before them. I want to thank my father (Robert Bankert) for giving me my my sense of integrity. It is something that I will always be grateful to him for. I want to thank my mother (Robin Hall) for always believing in me and giving me the self-confidence to reach for my dreams.

I want to thank my siblings, and there are quite a few of them. First of all Jestina, though we fought often as children, she is a good friend to me now that we have grown up. Jenna is always fun to hang out with, and I look forward to spending time with her whenever I am back home. Ally, though we may not be related by blood, you are every bit my sister. You are probably the only one in the family smarter than me :p. Jecinda's whimsical nature is always a treat, even though she usually has the dial set to 11. I know that you will do great things. Jared, you are my only brother and I wish that I had spent more time with you growing up. But, teenagers usually don't make the best life decisions, and that is one that I regret. I know that I can be hard on you sometimes, but that's just because I expect great things from you. To Akira (AKA Short-Round), you've got a great future ahead of you and I can't wait to see the person that you grow up to be. You may be too big to carry on my shoulders anymore, but that doesn't mean that I'll ever stop being your big brother.

I would also like to thank my step parents (Patrick Hall) and (Roxanne Bankert) for supporting me through the years both financially and personally.

To my best friend, (Mark Laczin) I want to thank you for all that you have done for me. We have been friends for nearly twenty years, and will be for many more. At this time, you are working towards your own PhD. Never give up, there is a light at the end of the tunnel, I am just beginning to see it for myself.

To Akvilina, I want to thank you for always being there for me. You are my partner through this life and I love you. The next few months will be hard as we must part ways for a little while, but we will be back together before you know it and we will have many wonderous years together.

Finally, I want to thank my advisor (Julian Krolik) for guiding me through this experience. I know that I haven't made it at all easy, but with your help, I have achieved this great thing.

Contents

List of Tables

List of Figures

Chapter 1 Introduction

1.1 Accretion Onto Compact Objects

A massive body exerts influence over nearby particles out to a distance where the particles' thermal energy is comparable to the gravitational binding energy of the body-particle system. Material within this region of influence is gravitationally attracted to the massive body, and unless another force overcomes gravity, accelerates towards it. That matter which impacts the massive body is said to accrete onto it.

The simplest accretion model is a spherically symmetric flow. However, this type of accretion requires that all gravitationally bound matter has zero angular momentum with respect to the central body. In real astrophysical systems, this is highly unlikely; a gravitationally bound gas cloud surrounding a central body usually has non-zero net angular momentum. As the cloud collapses, shocks at orbital stream crossings mix the gas's angular momentum and dissipate its kinetic energy. Minimizing kinetic energy, for a fixed angular momentum, puts the matter onto nearly circular orbits. Mixing angular momentum causes the circular orbits to settle into a coplanar disk surrounding the central body. The net angular momentum of the progenitor cloud determines the disk's orientation. For material within the disk to accrete, it must shed angular momentum. By transporting mass inwards and angular momentum outwards, the disk becomes an accretion disk.

1.2 Accretion Disk Angular Momentum Transport

Imagine a Keplerian accretion disk surrounding a point mass centered on the origin of a cylindrical coordinate system; the midplane of the disk is at $z = 0$ and the disk orientation such that only the z-component of the angular momentum is non-zero. In the radial direction, the disk has an angular velocity profile $\Omega = \sqrt{\frac{G\,M}{r^3}}$, where G is the Newtonian gravitational constant, and M is the mass of the central gravitating body. The time rate of change of the angular momentum within a thin annular shell ($dr \ll r$) of this accretion disk is given by:

$$\frac{\partial J_z}{\partial t} \;=\; \Delta \left[r^2 \int_{shell} (r\,\rho\,\Omega\,u_r - W_{r\phi})\; d\phi\, dz \right] + T_z \tag{1.1}$$

Here, J_z is the z-component of the angular momentum, $W_{r\phi}$ is the stress on the boundaries of the annular shell, $(r\,\rho\,\Omega\,v_r)$ is the advection of angular momentum through the annular shell boundaries, Δ indicates the difference between the inner and outer annulus boundaries, and T_z is any external torque. Understanding the nature of the stress induced torque was the forefront of accretion disk research in the latter part of the last century.

The most famous early model for angular momentum transport throughout an accretion disk was given by Shakura & Sunyaev (1973). They were uncertain of exactly how the stress arose, but they parameterized its effect by relating it to the gas pressure through a proportionality constant $-W_{r\phi} \sim \alpha\rho c_s^2 \;=\; \alpha\,P$. Here ρ is the gas density, c_s is the gas sound speed, and P is the gas pressure. They estimated α to be ≤ 1. This is known as the α model. In the next section, I discuss a more modern theory of angular momentum transport.

1.3 Magnetohydrodynamic Turbulence

In cgs (centimeter-gram-second) units, the equations which govern ideal magnetohydrodynamics (MHD) are:

$$\begin{aligned}
&\text{Continuity Equation:} && \frac{\partial \rho}{\partial t} + \vec{\nabla} \cdot (\rho \, \vec{v}) \;=\; 0 \\
&\text{Momentum Equation:} && \rho \left(\frac{\partial}{\partial t} + \vec{v} \cdot \vec{\nabla} \right) \vec{v} = -\vec{\nabla} \left(P + \frac{B^2}{8\pi} \right) + \left(\frac{\vec{B}}{4\pi} \cdot \vec{\nabla} \right) \vec{B} - \rho \, \vec{\nabla} \Phi \\
&\text{Faraday's Law:} && \frac{\partial \vec{B}}{\partial t} \;=\; \vec{\nabla} \times \left(\vec{v} \times \vec{B} \right) \\
&\text{Gauss's Law:} && \vec{\nabla} \cdot \vec{B} \;=\; 0
\end{aligned} \tag{1.2}$$

Here, all of the quantities are assumed to be the local values. ρ is the fluid's density, $\vec{v}$ is the fluid velocity, $\vec{B}$ is the magnetic field vector, P is the fluid pressure, and Φ is the gravitational potential. In these equations, we have assumed that the local microscopic viscosity is negligable. We now adopt a cylindrical coordinate system and consider only the azimuthal component of the velocity fields in the momentum conservation equation. Converting to a divergence form of the equations and rearranging yields:

$$\frac{\partial}{\partial t} \left(\rho \, v_\phi \right) \;=\; \vec{\nabla} \cdot \left[\frac{B_\phi}{4\pi} \vec{B} - \rho \, v_\phi \, \vec{v} - \left(P + \frac{B^2}{8\pi} \right) \hat{\phi} \right] \tag{1.3}$$

Focusing on changes in the radial direction, we get:

$$\frac{\partial}{\partial t}\left(\rho\, v_\phi\right) \;=\; \frac{1}{r}\frac{\partial}{\partial r}\left[r\left(\frac{B_\phi\, B_r}{4\pi} - \rho\, v_\phi\, v_r\right)\right] \tag{1.4}$$

We consider a thin Keplerian disk $\left(\Omega_{(r)} = \sqrt{\frac{G\,M}{r^3}}\right)$ and define the velocity perturbations to be the deviations from circular orbits: $u_r = v_r$, $u_\phi = v_\phi - r\,\Omega$ and $u_z = v_z$ with $\left(\frac{u_\phi}{r\,\Omega} \ll 1\right)$. Using these substitutions we volume integrate Equation 1.4 over the annulus. The fundamental theorem of calculus states that the radial integral of the radial derivative is simply the difference between the values on the shell boundaries of the annulus. Finally, multiplying both sides of the equation by the local radial coordinate leads to an expression for the conservation of angular momentum.

$$\frac{\partial J_z}{\partial t} \;=\; \Delta\left[r^2 \int_{shell}\left(r\,\rho\,\Omega\,u_r + \frac{B_\phi\, B_r}{4\pi} - \rho\, u_\phi\, u_r\right)\right] d\phi\, dz \tag{1.5}$$

From this we can see that the stress tensor born from magnetohydrodynamic turbulence is a combination of two different stresses $W_{r\phi} = M_{r\phi} + R_{r\phi}$.

$$\begin{aligned} &\textbf{Maxwell Stress}: \quad M_{r\phi} \;=\; -\frac{B_r\, B_\phi}{4\pi} \;=\; -\rho\, v_{A,r}\, v_{A,\phi} \\ &\textbf{Reynolds Stress}: \quad R_{r\phi} \;=\; \rho\, u_r\, u_\phi \end{aligned} \tag{1.6}$$

Here, v_A is the Alfven velocity. More information can be found in Balbus & Hawley (1998) who discuss this topic in much greater depth.

It is important to understand how the magnetic field within an accretion disk may grow strong enough for the Maxwell stress to play a major role in angular momentum transport. To that end, we will now discuss a widely recognized growth mechanism

for Keplerian-like disks.

1.3.1 Magnetorotational Instability

Balbus & Hawley (1991) showed that the magnetorotational instability (MRI) can create MHD turbulence, which in turn is a mechanism for magnetic field growth. To gain an intuition for the nature of the instability, consider Figure 1.1 and Figure 1.2 . These figures depict a disk of partially ionized gas whose rotation rate decreases with increasing radius. Figure 1.1 shows a cross-sectional view through one side of this hypothetical disk, while Figure 1.2 shows a top-down view. In the initial condition, a vertical magnetic field (B_z) threads the disk **(1)**. Now, we displace a fluid element radially by a small amount ($\delta r \ll r$). According to Alfven's theorem, magnetic field lines, which thread an infinitely conducting fluid, are "frozen" into the fluid and cannot move independently of it. Movement of the magnetic field lines would induce movement of the fluid and vice versa. This condition defines "ideal" magnetohydrodynamics (MHD). However, a plasma is still able to couple to embedded magnetic fields even when the ionization fraction is small Blaes & Balbus (1994). Thus the displacement of the fluid element stretches the vertical magnetic field, producing a radial magnetic field component **(2)**. Due to the Coriolis force acting on the displaced fluid element, the angular velocities of the fluid elements now vary radially along the disturbed magnetic field line. The field line then stretches azimuthally as the disk rotates, and a perturbed (B_ϕ) field is produced **(3)**. The tension in the disturbed magnetic field line transfers angular momentum outward from the fluid elements at lower radial orbits to those at higher radial orbits. A fluid element, which loses angular momentum, will move radially inward. Likewise, a fluid element, which gains angular momentum, will move radially outward. This

increasing separation of fluid elements, which are threaded by the same magnetic field line, enhances the original perturbations **(4)**, and leads to an instability. This magnetic field growth drives MHD turbulence which is the dominant mechanism for angular momentum transport throughout an accretion disk (Balbus & Hawley, 1998).

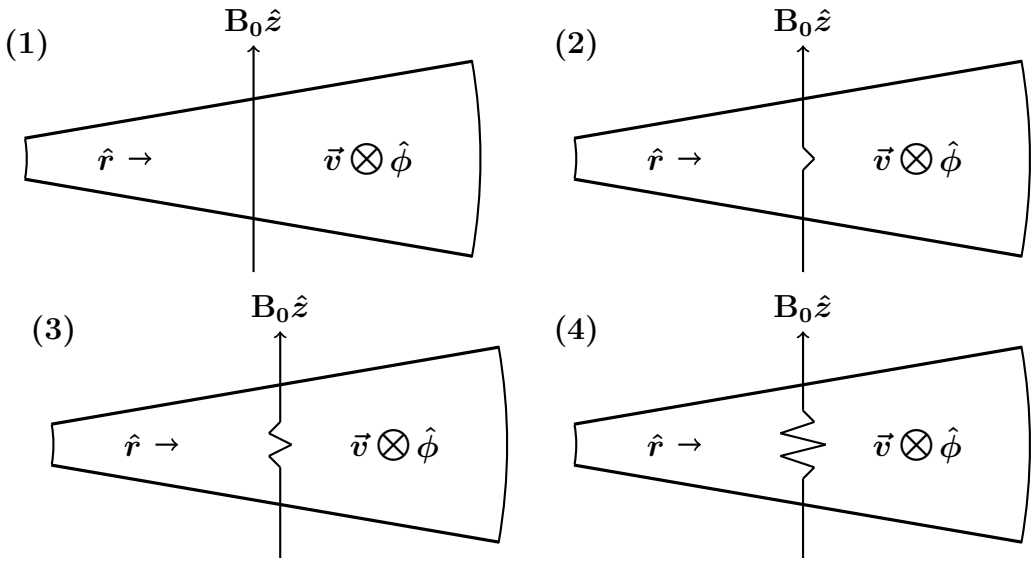

Figure 1.1: Model Disk: Side View

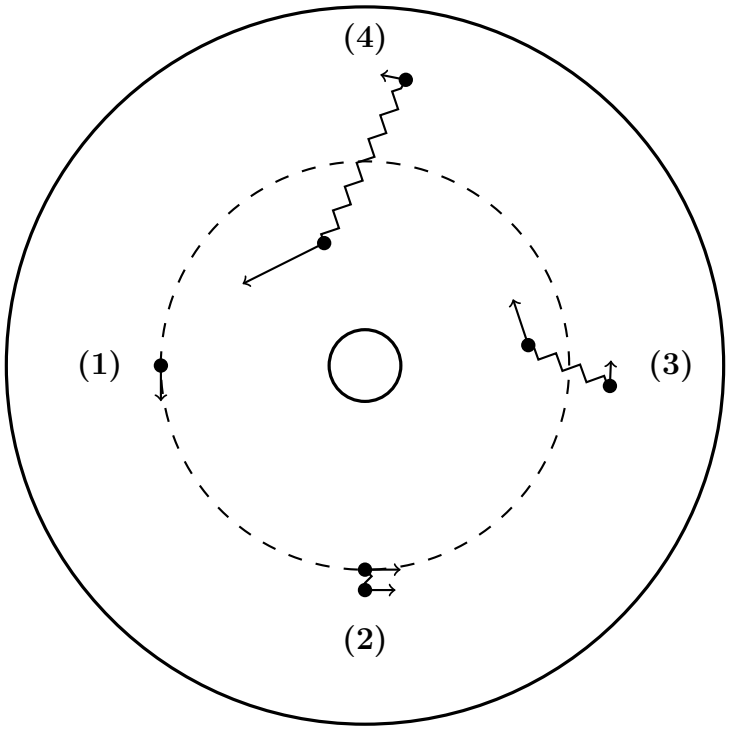

Figure 1.2: Model Disk: Top-Down View. Distances exagerated for effect.

1.4 Circumbinary Accretion Disks

An astronomical binary with a large reservoir of gravitationally bound gas (such as protostars embedded in the remains of their progenitor cloud or supermassive black holes capturing gas from their host galaxy) will develop a circumbinary accretion disk when dissipative shocks in orbital stream crossings cause the gas particles to mix orbital angular momentum and lose orbital energy. By the laws of conservation, the net orientation of the forming disk will be governed by the total angular momentum of the progenitor gas cloud. It is very unlikely that the initial disk orientation will be either exactly co-aligned (prograde) or anti-aligned (retrograde) with the binary's orbital plane. However, recent work by (Nixon, 2012; Sorathia et al., 2015; Miller & Krolik, 2013) gives reason to believe that the inner regions of the disk will either

co-align (forming a prograde disk) or anti-align (forming a retrograde disk) with the binary's orbital plane on time scales that are much shorter than the those that govern the binary's evolution.

Circumbinary disks play an important role in theories of astronomical binary system evolution for a large range of masses, from sub-solar mass stars to supermassive black hole binaries (SMBHBs). Protostellar disks surround forming stellar systems. In these cases, the circumbinary disk plays a significant role in the formation of planetary bodies and multiple star systems (Papaloizou & Lin, 1984; Krumholz et al., 2009; Martin et al., 2016). SMBHBs are expected to be found in the cores of post-merger galaxies (Begelman et al., 1980; Volonteri et al., 2003; Mayer et al., 2007; Dotti et al., 2009). Through 3-body interactions with the surrounding stars, SMBHBs can shed angular momentum and shrink their orbit to a scale of approximately a parsec (Milosavljević & Merritt, 2001). After this point, the region around the binary is generally too depopulated for 3-body stellar interactions to continue to be a viable mechanism for binary shrinkage. It remains unclear which mechanisms dominate a SMBHB's orbital evolution while its separation is smaller than a parsec, but still too large for gravitational radiation to cause binary coalesance on a timescale shorter than the Hubble time. This is known as the final parsec problem. Recent studies of binary evolution via encounters with stars suggests that in the aftermath of a galaxy merger, the stellar distribution is very likely triaxial. In this state, it is easy to keep the stellar loss-cone filled (Volonteri et al., 2003; Milosavljević & Merritt, 2003; Merritt & Poon, 2004; Vasiliev et al., 2013, 2015). Another possibility is interactions with surrounding gas, when enough is available, (Gould & Rix, 2000; Armitage & Natarajan, 2002; Escala et al., 2004, 2005; MacFadyen & Milosavljević, 2008; Cuadra et al., 2009).

There are two primary mechanisms of binary-disk interaction: gravitational torques

and mass accretion. Gravitational torques exchange angular momentum and energy between the binary and the disk. Matter accretion from the inner edge of the disk onto the binary adds both the mass, angular momentum, and energy of the accreted material to the binary. The change in binary mass also modifies the potential energy of the binary system. A prograde disk is co-aligned with the binary's orbit, thus matter accreted from the disk increases the binary's angular momentum. Conversely, as a retrograde disk is anti-aligned with the binary's orbit, matter accreted from the disk decreases the binary's angular momentum.

To understand the differences between prograde and retrograde disks, it is worthwhile to turn to linear resonance theory (in which the ratio of secondary to primary mass $q \ll 1$). In this case, the torques can be understood through Lindblad resonances (Goldreich & Tremaine, 1980; Papaloizou & Lin, 1984; Meyer-Vernet & Sicardy, 1987; Artymowicz & Lubow, 1994, 1996). Framed in this way, it becomes immediately clear that retrograde disks cannot support such resonances, and are therefore likely to interact very differently with a central binary than prograde disks. Computer simulations have shown that prograde and retrograde disks will interact differently with a central binary even in the nonlinear regime of $q \sim 1$ (Nixon et al., 2011a). Indeed, the magnitude of binary-on-disk torques is much greater for prograde disks than for retrograde disks (Nixon et al., 2011a; Bankert et al., 2015) also (Roedig & Sesana, 2014) (Hereafter RS14). In the case of a binary that has a mass ratio near unity, the disparity in the magnitude of the applied torques creates a distinct morphological difference between prograde and retrograde disks. A retrograde disk extends all the way to the binary, while a central gap region forms in a prograde disk. For a binary on a circular orbit, the prograde gap region extends out to approximately twice the binary separation distance (Pringle (1991); Artymowicz & Lubow (1994, 1996); Shi

et al. (2012) (Hereafter SK12); MacFadyen & Milosavljević (2008); Miranda et al. (2016)).

The differences between prograde and retrograde disk structure for near unity mass ratio binaries result in different means of accretion. In the retrograde case, matter accretes directly from the inner edge of the disk onto the binary (RS14, Bankert et al. (2015)). The strong gravitational torques which create the gap region in a prograde disk prevent direct accretion onto the binary. Accretion still occurs, however, when streams of material peel off of the inner edge of the circumbinary disk. The gravitational torques which form the gap region eventually repel much of the stream material back toward the bulk disk, but a small amount can accrete onto the binary. This was first discovered by Artymowicz & Lubow (1996), and has since been observed by many others (e.g. MacFadyen & Milosavljević (2008), SK12, Noble et al. (2012); Farris et al. (2014)) and (Shi & Krolik, 2015) (Hereafter SK15)). SK15 determined that the criterion for gas to be able to pass through the gap into the binary region is for the gas particles to have less than a certain fraction of the Keplerian momentum $\frac{j_{gas}}{\Omega_{bin}\, a^2} \leq \mathscr{C}$. They found $\mathscr{C}$ to be 1.3 for a binary on a circular orbit (They also found that $\mathscr{C} \leq 1.5$ is acceptable if the gas particle had high enough inward radial velocity.) The production of a population of fluid elements that meet these criterion is driven by binary torques which repel material in the gap region (which is not already on course to be accreted) outward towards the main disk. This material forms shocks as it impacts the main disk, and a portion of shocked fluid loses enough angular momentum to fit the criterion for accretion.

(Roedig et al., 2012) found in prograde disks that even though torques act to remove angular momentum from the binary, the angular momentum gained through the accretion of material was enough that the net effect was an increase in the binary's

orbital angular momentum. RS14 investigated the evolution of SMBHBs embedded in both prograde and retrograde circumbinary disks. They found that, for circular orbit binaries, there was little change in eccentricity for a binary surrounded by a retrograde disk, but there was a noticeable change for a binary surrounded by a prograde disk. It is important to note however, that they did not develop accretion mini-disks in their retrograde circumbinary disk runs, which has profound implications for the manner in which matter accretes onto the black holes. Furthermore, their analysis, was based on simulations which utilized smooth particle hydrodynamics and internal stresses due to disk self-gravitation to emulate the circumbinary disk. Balbus & Hawley (1991) showed that magnetohydrodynamics (MHD) plays a crucial role in the internal dynamics of weakly magnetized accretion disks. Thus, since the evolution of the central binary is very sensitive to the accretion rate of the disk, it is necessary to investigate the problem using a disk modeled with MHD.

Chapter 3 is based on the paper Bankert et al. (2015). The goal of this research was to study in detail how retrograde circumbinary disks differ from prograde disks. Others (Nixon et al. (2011a); RS14) have also engaged in such an effort. Ours differs from previous work by incorporating MHD stresses stirred by the magneto-rotational instability in order to drive accretion. By contrast, Nixon et al. (2011a) assumed a hypothetical "α"-viscosity, while RS14, although similarly eschewing a hypothetical viscosity mechanism, instead assumed a disk mass great enough to make self-gravitational torques the principal mechanism of accretion. We also differ from previous work by looking more closely at the properties of the disks themselves. Among the properties we will examine quantitatively are: their radial surface density profiles in the range $a \lessapprox r \lessapprox 4a$, where prograde disks generically have a surface density peak outside a gap; their efficiency conveying accretion flows onto the binary;

potentially observable distinctive signals. We also comment on the long-term evolution of such a system, but leave detailed analysis to a companion paper. We also postpone to future work considerations having to do with evolution of the orbital plane in the event that the circumbinary disk does not lie precisely in the plane of the binary and supplies an amount of mass large enough to contribute noticeably to the total angular momentum of the system (Nixon et al., 2011b).

In the eccentric binary research we investigate prograde circumbinary accretion disks around equal mass binaries on fixed eccentric orbits. We do this by using 3D, MHD simulations (in the fashion of SK12, Bankert et al. (2015), Shi & Krolik (2015)) to model prograde circumbinary disks in orbit around a central binary on a variety of eccentric orbits ($e = 0.2$, $e = 0.4$, $e = 0.6$, $e = 0.8$). Others have investigated this problem using purely analytical methods (Rafikov, 2016), smooth particle hydrodynamics (SPH) with either an artificial α viscocity model (Goicovic et al., 2016) or a self-gravitating disk (Roedig et al., 2012), or 2D hydrodynamics (Miranda et al., 2016).

For this work our goals are: (1) Understand the evolution of the binary's orbital characteristics (semi-major axis a and eccentricity e). (2) we explore the orbital phase dependence of mass accretion, binary torque, binary angular momentum evolution, and binary energy evolution in order to gain a better understanding of the nature of accretion onto eccentric binaries. We believe that we are the first to do a detailed investigation into the orbital phase dependence of the aforementioned quantities for eccentric binaries.

Chapter 2 Methods

2.1 Zeus Code

Our simulations used an updated version of the Zeus code (Stone & Norman, 1992a,b), rewritten in Fortran95 by John Hawley and Kris Beckwith. The code was modified by Ji-Ming Shi to incorporate a central binary gravitational potential (SK12). The code was further updated by Justin Bankert to allow for the gravitational potential of an eccentric binary.

The Zeus code operates in the regime of Newtonian physics, which is acceptable for our purposes, because we are interested in the evolution of general binary-disk systems at all mass scales, and in the case of black hole systems we are interested in the time before gravitational waves dominate the binary's evolution. The code also employs ideal magnetohydrodynamics, which is an appropriate approximation as the disk fluid will be well coupled to the magnetic field even for a cool disk with a small ionization fraction. The Zeus code uses a MOC-CT (method of characteristics plus constrained transport) algorithm to ensure that $\vec{\nabla} \cdot \vec{B} = 0$ in a way that evolves the disk's magnetic field in a conservative fashion $\left(\frac{\partial \Phi}{\partial t} = \oint (\vec{v} \times \vec{B}) dl \right)$. Zeus also uses finite-differencing algorithms to evolve disk fluid by solving the continuity equation and the momentum equation of Equation 1.2 .

2.2 Physical Model

Our simulations utilized the gravitational potential of an equal mass ratio binary. The binary's center of mass defined the origin of the computational grid, and its orbital plane was identical to the midplane of our spherical coordinate system. In Chapter 3 the binary was fixed on a circular orbit, while in Chapter 4 the binary was set on a variety of elliptical orbits e =(0.0, 0.2, 0.4, 0.6, 0.8). In both cases, the binary's orbit was frozen for the duration of the simulation. This orbit freezing is an excellent approximation because the disk dynamical timescale is much smaller than the binary shrinkage timescale, and in both cases we ran the simulation for a relatively short time, between 70 and 100 binary orbits.

To create physically meaningful unitary length and time scales, our code units define the gravitational constant (G), total binary mass ($M = M_1 + M_2$), and the semi-major axis of the binary's orbit (a) to be unity. Thus the unitary length scale is (a), and the unitary time scale is the inverse of the binary's orbital frequency $\tau = \frac{1}{\Omega_{bin}} = \sqrt{\frac{a^3}{G\,M}}$.

We approximate a cold, moderately thin disk and use a global isothermal sound speed of $c_s = 0.05\times$ the inverse of the binary's orbital frequency. Although thin, the disk will flare slightly at large radii. The disk's scale height as a function of radial position is $\frac{H}{r} \approx \frac{c_s}{r\,\Omega_K} = 0.05\,\left(\frac{r}{a}\right)^{-1/2}$, where $\Omega_K = \sqrt{\frac{GM}{r^3}}$ is the Keplerian frequency. We assume ideal MHD, since the fluid in a cold disk still couples well to a magnetic field even when the ionization fraction is small. Therefore, we do not include any explicit diffusivity, except the von Neumann-Richtmyer bulk viscosity in compressive regions in order to maintain the correct jump conditions across shock boundaries. By assumption, the disk's mass is negligible compared to the binary mass.

For Chapter 3 and (SK12), the initial disk extends radially from $3a$ to $6a$ with the density constant in the mid-plane for all radii and azimuthal angles. The vertical density distribution was set in order to ensure hydrostatic equilibrium. The orbital angular frequency of the disk was modified to account for the binary potential:

$$\Omega^2{}_{(r)} \;=\; \Omega^2_{\rm bin}\left(\frac{a}{r}\right)^3\left[1+\left(\frac{3}{16}\right)\left(\frac{a}{r}\right)^2\right]+\frac{1}{(r\Sigma)}\frac{dP}{dr} \tag{2.1}$$

The pressure gradient term on the right-hand side is added to compensate for the small radial gradient of the vertically integrated pressure ($\mathrm{P} = \Sigma c_s^2$).

The initial magnetic field is a family of nested poloidal field loops following the density contours of the disk. This field is sub-thermal, with the plasma $\beta \sim 100$; the related quantity $\langle p\rangle/\langle B^2/8\pi\rangle = 100$. It is determined from a vector potential whose sole non-zero component is azimuthal:

$$A_\phi \;=\; \max\left[0, A_0\sqrt{\rho}\,\sin\left(\frac{2\pi r}{kH}\right)\left(\frac{r}{r_{\rm min}}-1\right)\left(1-\frac{r}{r_{\rm max}}\right)-\sqrt{\rho_{\rm cut}}\right] \tag{2.2}$$

Here $k = 2\,\Omega_{\rm bin}a/c_s$, $\rho_{cut} = 10^{-3}\rho_0$, and A_0 is a constant determined by the constraint on the average plasma β.

For Chapter 4 , we use the data from (SK12) as an initial condition for each of our simulations. Using the data produced by their simulation as an initial condition is no less physically accurate than those which we previously described and which were used by (SK12) and by us in Chapter 3 . Further, by starting with a disk that has already evolved away from a perfectly axis-symmetric torus, we save on computational time.

It is important to note that the branch point from which our simulations emerge from their data occurs before the formation of the large, non-axis-symmetric surface density feature which they label the "lump".

2.3 Grid Scheme

We used the spherical coordinate grid proposed in (Noble et al., 2010). In the radial direction, $\frac{\Delta r}{r} = 0.007333$ is kept constant to produce a logarithmic radial mesh, running from $r_{\rm in} = 0.8\,(1+e)\,a$ to $r_{\rm out} = 15a$. The polar angle grid is constructed by:

$$\theta_i \;=\; \frac{\pi}{2}\left[1 + (1-\zeta)\left(\frac{2\,i}{N_\theta} - 1\right) + \left(\zeta - \frac{2\,\theta_c}{\pi}\right)\left(\frac{2\,i}{N_\theta} - 1\right)^n\right] \tag{2.3}$$

Here, i denotes the cell index, $N_\theta = 160$ is the number of grid cells in the polar angle direction, and the parameters $\zeta = 0.9$, $\theta_c = 0.2$, and $n = 9$ control the concentration of cells near the midplane. The entire range of azimuthal angles is covered with 540 equally spaced cells. With these choices, the range of covered runs from 0.2 to $\pi - 0.2$ radians.

We chose this grid scheme to resolve the length scales relevant to three different physical processes. The first is the vertical hydrodynamical scale height (H) of the disk above the midplane. To resolve this, we use several tens of polar angle cells per H for a few scale heights around the midplane. Secondly, we must resolve the acoustic waves within the disk plane, which are driven by the binary's orbit. These have a wavelength of $\lambda_d = 2\pi\frac{c_s}{\Omega_{bin}}$. We require there to be > 10 radial cells per wavelength for $r < 4a$ and > 6 cells per wavelength for $r < 7a$. Lastly, we resolve the MHD

turbulence driving accretion. To accurately portray linear growth, the criterion is at least six cells per fastest-growing vertical wavelength (Sano et al., 2004). A stricter standard is required to follow the nonlinear development of the turbulence, both quality factors $Q_z = 2\pi v_{Az}/(\Omega r \Delta\theta)$ and $Q_\phi = 2\pi v_A/(\Omega r \Delta\phi)$ must be $\gtrsim 10$, where v_{Az} is the Alfven speed with respect to the vertical component of the magnetic field and v_A is the Alfven speed with respect to the total field (Hawley et al., 2011; Sorathia et al., 2012).

2.4 Computational Domain

Using $N_r(=400) \times N\theta(=160) \times N_\phi(=540)$ cells, the computational domain covers the region: $r\,\epsilon\,[0.8\,a(1+e), 15a]$, $\theta\,\epsilon\,[0.2, \pi - 0.2]$, $\phi\,\epsilon\,[0, 2\pi]$. The location of the inner radial boundary was chosen to excise the region containing the binary and any inner accretion disks surrounding the individual binary members; treating the fluid dynamics within the inner disks would demand a large increase in computational resources. For the investigation of eccentric binaries, the inner radial boundary is expanded with eccentricity, to ensure that the binary remains within the cutout region even when at apoapsis. The location of the outer radial boundary was chosen to permit a reasonable radial dynamic range. The polar angle edges were chosen to be well off the plane but far enough from the polar axis so that there were no exceedingly small cells. Outflow boundary conditions were imposed along all of these surfaces; any velocity pointing into the computational domain on these surfaces was set to zero. The magnetic field boundary condition on these surfaces was that all transverse components were set to zero in the ghost cells, while the field components normal to the surface were determined by imposing the divergence-free condition. All quantities were set to match across the periodic boundary in the azimuthal direction.

Chapter 3 Retrograde Disks

It is the goal of this research to study in detail how retrograde circumbinary disks differ from prograde disks. We also examine closely the properties of the disks themselves. Specifically, we examine: their radial surface density profiles in the range of $a \lesssim r \lesssim 4a$, where prograde disks generically have a non-axissymetric "lump" feature; their efficiency in conveying accretion flows onto the binary; potentially observable distinctive signals. Finally, we comment on the long-term evolution of such a system, but leave detailed analysis to a companion paper.

Our simulation ran for approximately 600 time units. This runtime corresponds to just under a hundred binary orbits. Within the first 70 time units, just over 10 binary orbits, the inner edge of the initial disk moved all the way to the inner boundary of the computational grid. As angular momentum propagated through the disk, the outer edge of the disk expanded outwards. By the end of the simulation, the inner regions of the disk had reached a state of quasi-steady accretion; as Figure 3.5 shows, by that point the time-averaged mass accretion rate changes hardly at all from the inner boundary to $r \simeq 2$. However, larger radii are significantly out of inflow equilibrium as the time-averaged accretion at $r \gtrsim 3$ is approximately double its value in the inner disk.

3.1 Disk Structure

A key aspect of understanding retrograde circumbinary disks is to contrast them with prograde disks. Because everything about the set-up of our retrograde simulation matched the prograde simulation of SK12 with the exception of the direction of rotation, it is natural to use the SK12 work as our comparison standard. When we compare to prograde disks, we use exclusively data from SK12.

3.1.1 Density Profile

In Figure 3.1 we show azimuthally-averaged surface density profiles and surface density snapshots for both these simulations. After an initial transient period, the inner edge of the retrograde disk nearly reaches the inner edge of the computational domain. Its surface density distribution remains relatively flat out to $r \approx 3a$, but falls at larger radii. We caution that there may be boundary artifacts in the shape of the surface density profile for $r \lessapprox a$, but we expect that $\Sigma_{(r)}$ is accurately determined at larger radii. This behavior contrasts strongly with the prograde case, in which the surface density profile has a sharp peak at $r \approx 2a$ and falls to very low values at smaller radii. There are transient streams inside $r \approx 2a$ in the prograde case, but their azimuthally-averaged surface density is much smaller than in the main body of the disk outside $r \approx 2a$.

Our results in this aspect are qualitatively similar to those of RS14, but quantitatively are modestly different. Although we find a peak in surface density in the retrograde case at $r \simeq 2a$, it is not appreciably greater than the surface density at $r \simeq a$; at still smaller radii, we find the surface density declines rapidly, but as just remarked, some of this decline may be a boundary artifact. RS14, on the other hand,

find a very sharp decline in surface density for $r < 1.5\,a(1+e)$. In another striking contrast with the prograde circumbinary disks studied by (SK12, Noble et al. (2012), and Farris et al. (2014), which all developed a very large non-axisymmetric feature they dubbed the lump, the retrograde case never developed any large departures from axisymmetry. SK12 attributed the growth of the lump to the portions of the accretion streams redirected outward by strong binary torques; here there are no streams and no torque (as we will show quantitatively momentarily), so there is no growing lump.

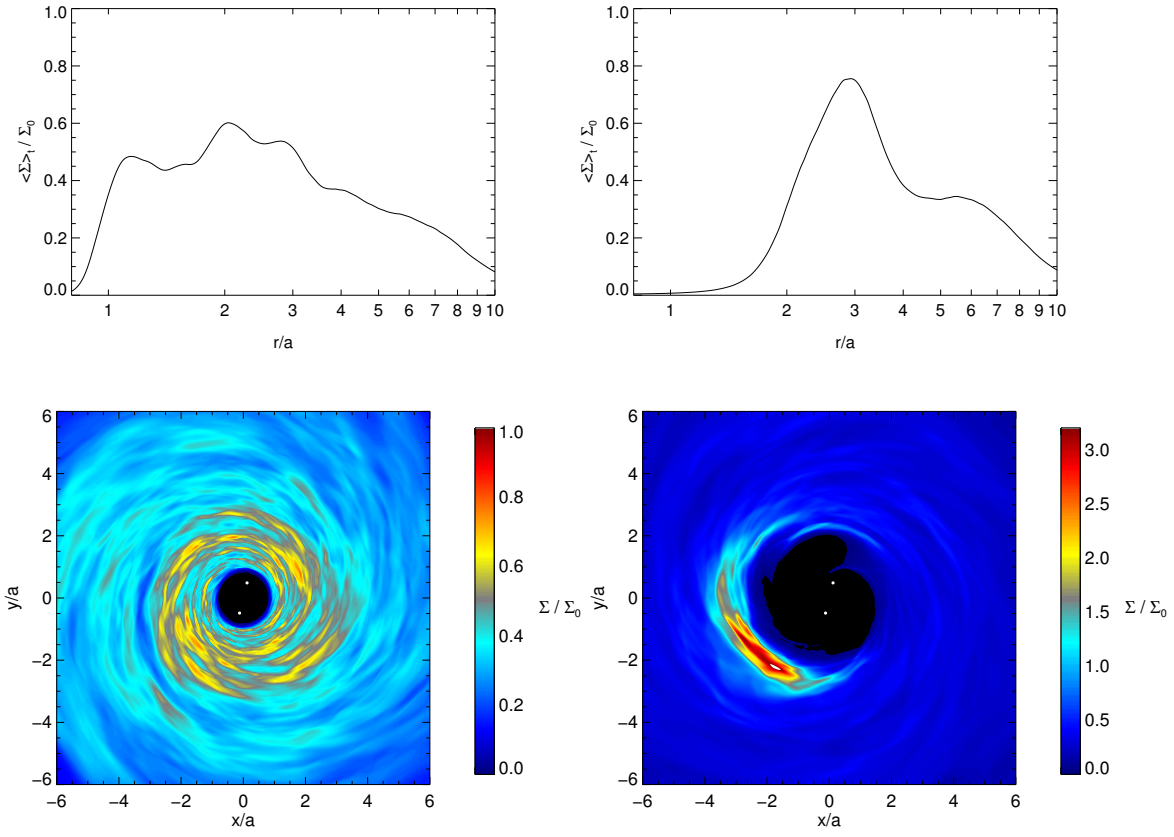

Figure 3.1: Top row: time- and azimuthally-averaged surface density. Left: retrograde, averaged over $500 \leq t \leq 563$. Right: prograde, averaged over $400 \leq t \leq 463$. Bottom row: snapshots of surface density at $t = 460$ in both cases. Note the very different color scales of the two bottom row figures.

3.1.2 Spiral Features

At late times (t $\sim$ 400 and later), spiral perturbations in the surface density are present in both sorts of cirumbinary disks. In the retrograde disk, these perturbations continue to be present even to very small radii. In the prograde disk, however, the binary torques carve a gap inside $r \simeq 2a$, and within the annulus $2a \lesssim r \lesssim 4a$, the surface density structure is dominated by the lump pointed out by SK12. As just shown, the azimuthally-averaged surface density structure of the two cases becomes similar outside $r \sim 4a$, but in principle the nature of smaller-scale perturbations might differ. To answer this question, we compare them over the range $4a < r < 10a$, with the outer limit chosen because neither disk is fully relaxed at $r > 10$ a even at t $\sim$ 400. For contrast enhancement, we study the perturbations in this radial range after subtracting the time- and azimuthally-averaged surface density Figure 3.2 . Qualitatively, the spiral features of both prograde and retrograde disks seem very similar.

To quantify the amplitudes of the perturbations, we compute $\left\langle \frac{\delta\Sigma}{\Sigma} \right\rangle_\phi$:

$$\left\langle \frac{\delta\Sigma}{\Sigma} \right\rangle_\phi^{(r)} = \sqrt{\frac{1}{2\pi\, T} \int_t \int_0^{2\pi} \left(\frac{\Sigma_{(r,\phi,t)}}{\langle\Sigma\rangle_{\phi\,(r,t)}} - 1 \right)^2 d\phi\, dt} \tag{3.1}$$

Here the averaging period T was two binary orbits centered on t = 450. These data are displayed in Figure 3.3 , where it is apparent that at radii sufficiently outside the surface density maximum of the prograde case, the amplitude of the perturbations is similar, but not identical, in the two cases. In those outer regions, the retrograde rms fractional fluctuation is consistently $10 - 15\%$ of the mean surface density; in the prograde case, the amplitude is similar for $4a \lesssim r \lesssim 7a$, but rises at larger radii,

reaching $\simeq 20\%$ at $r \simeq 10a$. Whether this contrast is significant or merely a statistical fluctuation is difficult to determine.

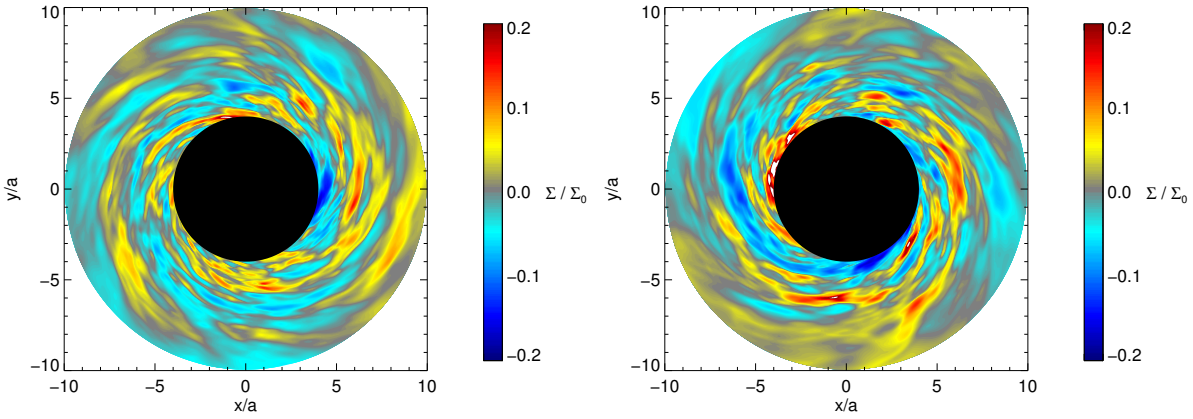

Figure 3.2: The difference in surface density between a snapshot at $t = 400$ and the azimuthally-averaged surface density profile averaged over the two orbits centered on the time of the snapshot. Regions outside the range $4a \leq r \leq 10a$ are masked. Left: retrograde; right: prograde.

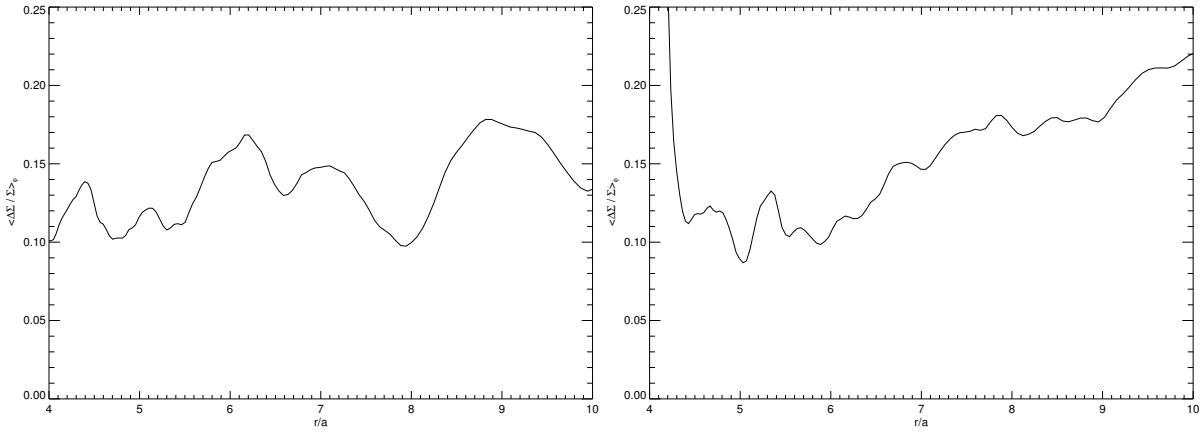

Figure 3.3: $\frac{\Delta\Sigma}{\Sigma}$ over the range $r = 4a$ to $r = 10a$. Left: retrograde; right: prograde. The sharp rise in $\frac{\Delta\Sigma}{\Sigma}$ in the prograde disk at $r \sim 4a$ occurs because this is the beginning of the region dominated by the lump.

3.1.3 Disk Eccentricity

Earlier studies of prograde circumbinary disks (MacFadyen & Milosavljević (2008), SK12) found that, beginning from perfectly circular orbits, they grow in eccentricity. This growth (in logarithmic terms) is rapid during the first several tens of orbits, then slows at later times, but continues. We can test whether anything similar occurs in retrograde disks by measuring the disk eccentricity as defined by SK12:

$$e_{\rm disk} = \frac{1}{P_{\rm bin}} \int_t^{t+P_{\rm bin}} \frac{\left| \int_{r_1}^{r_2} \int_{\theta,\phi} \rho\, v_r\, e^{i\,\phi}\, r^2 \sin(\theta)\; d\theta\, d\phi\, dr \right|}{\int_{r_1}^{r_2} \int_{\theta,\phi} \rho\, v_\phi\, r^2 \sin(\theta)\; d\theta\, d\phi\, dr}\, dt' \qquad (3.2)$$

Here P_{bin} is the binary period, and r_1 and r_2 are the bounds on the region containing most of the disk mass ($r_2 = 5a$ for both, but $r_1 = 0.8a$ for the retrograde disk and $2a$ for the prograde). Figure 3.4 illustrates the similarities and the contrasts between the two cases. At first, the eccentricity grows rapidly from nil for both prograde and retrograde orbital motion. By $t \simeq 100$ ($\simeq 15$ orbits), however, e_{disk} levels off at $\simeq 0.002$ in the retrograde disk. In contrast, e_disk in the prograde case continues growing, although more slowly than during the period $t \lesssim 100$.

We believe the early growth of eccentricity in both cases is the result of small departures from equilibrium in the initial conditions that cause small radial motions. This sort of noise appears to be capable of creating eccentricity at the saturation level observed in the retrograde case, $\simeq 0.002$. SK12 attributed the growth of eccentricity in the prograde case beyond this level to the same stream reattachment that also drives the growth of the lump. Once again, the absence of interior streams in the retrograde case can explain the cessation of eccentricity growth in the retrograde case.

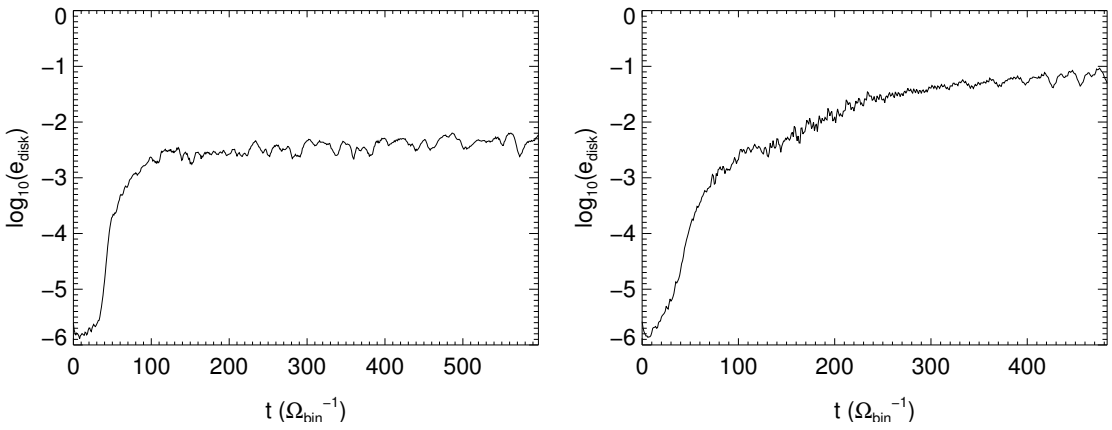

Figure 3.4: Growth of disk eccentricity with respect to time. Left: retrograde; right: prograde.

3.2 Accretion

On the basis of an essentially one-dimensional model, Pringle (1991) and Nixon et al. (2011a) argued that binary torques operating on a prograde circumbinary disk transform it from an accretion disk to a "decretion disk," one in which there is essentially no accretion inside $r \simeq 2a$. However, recent two- and three-dimensional simulational work has shown that a sizable fraction of the accretion rate at large radii is, in fact, transmitted to the binary. This fraction is almost certainly at least $\sim O(0.1)$ and may be $\sim O(1)$ (MacFadyen & Milosavljević (2008); Roedig et al. (2012); SK12; RS14; Farris et al. (2014)).

In Figure 3.5 we compare the radial dependence of the accretion rate with that of SK12. In both cases the time-averaged accretion rate through the inner boundary is roughly $0.015\,\Omega_{bin}\,\Sigma_0\,a^2$, suggesting that the net accretion rate is at most weakly dependent on the sign of disk orbital motion; using a very different simulational method, RS14 found a very similar result. However, as is clear from looking at the variations in accretion rate with radius at larger r, neither system can truly be said

to be in inflow equilibrium. Consequently, this approximate equality is only that. Such an imperfect state of inflow equilibrium makes evaluation of the fraction of the mean accretion rate at large radius transmitted to the binary necessarily uncertain, although it is apparent that this fraction is not small.

A sense of the range of fluctuation in the accretion rate in both cases can be obtained from Figure 3.6 . It is clear from a comparison of these two figures that their mean accretion rates are similar, and there is some resemblance in their long-term behavior, but the short-term time-dependence of the two cases is quite different. In both cases, the accretion rate is in the range $\simeq (0.01 - 0.04)\,\Omega_{bin}\,\Sigma_0\,a^2$, exhibits an early-time peak ($t \simeq 100-150$), a local minimum at $t \simeq 200$, a smaller local maximum at $t \sim 300-400$, and falls to $\simeq 0.01\,\Omega_{bin}\,\Sigma_0\,a^2$ at $t \simeq 500$. On the other hand, there is much greater high-frequency fluctuation power in the prograde case. As discussed by SK12, the high-frequency fluctuations are largely due to resonances with the binary orbital frequency, an effect that we have already pointed out is entirely absent from the retrograde case.

Our simulation does not deliver material passing through the inner boundary to the binary. However, we may safely assume that, in the case of a real binary system, this material would be accreted onto the binary. Its effect on the binary's orbit depends on the specific energy and angular momentum carried to the binary. As we will discuss later, when matter is captured by one or the other member of a real binary, all the angular momentum is delivered to the binary orbit, but some of the energy will likely be lost to radiation. In any event, the mean accreted angular momentum per unit mass is very close to $-1.25\,\Omega_{bin}\,a^2$, with fractional fluctuations in time of only $\simeq 1\%$. Interestingly, it is slightly more negative than the mean specific angular momentum at the inner boundary, $\simeq -1.21\,\Omega_{bin}\,a^2$ (this is noticeably greater

in magnitude than the Keplerian circular angular momentum at $r = 0.8a$ because of the quadrupolar contribution to the potential). The mean accreted orbital energy per unit mass is -0.54, averaged over the period $500 \leq t \leq 563$.

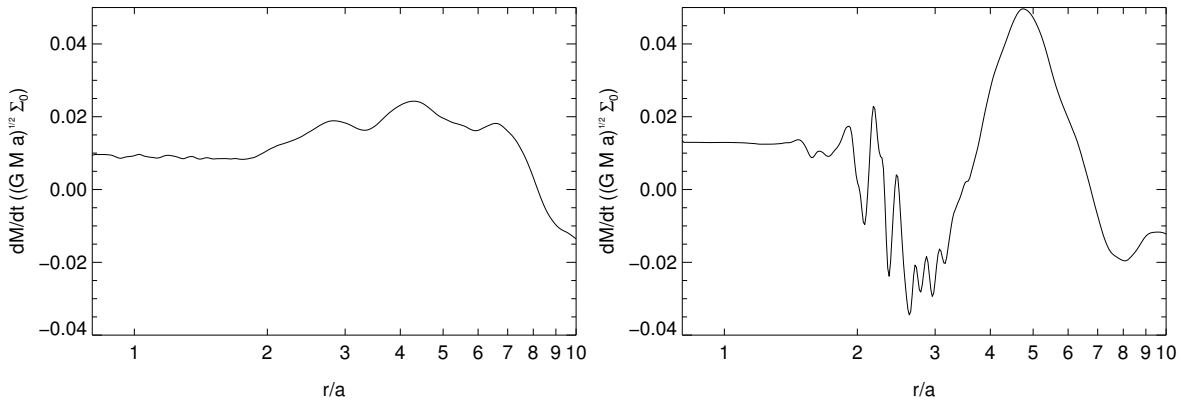

Figure 3.5: Vertically-integrated, azimuthally- and time-averaged accretion rates as a function of radius. Left: retrograde, averaged over $530 \leq t \leq 593$; right: prograde, averaged over $420 \leq t \leq 483$.

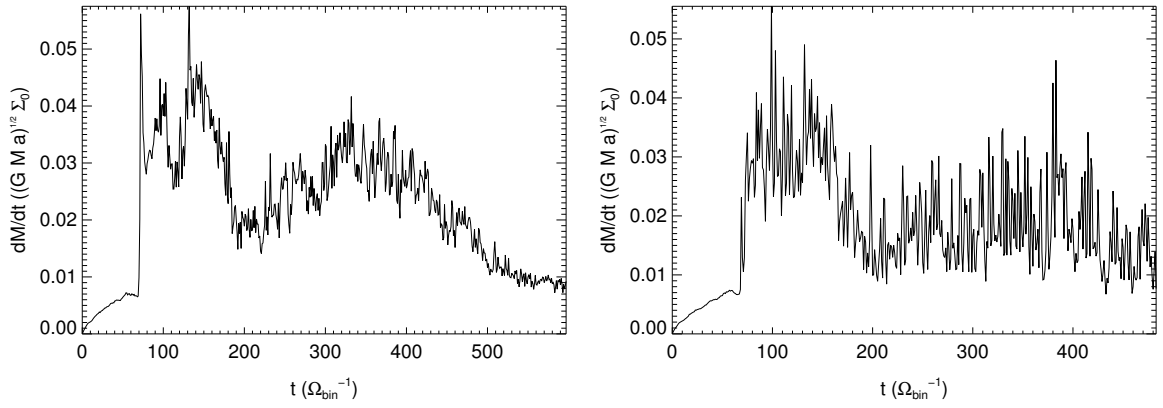

Figure 3.6: Accretion rate through the inner boundary as a function of time. Left: retrograde; right: prograde.

3.3 Torque

As discussed by many (Papaloizou & Pringle, 1977; Goldreich & Tremaine, 1980; Papaloizou & Lin, 1984; Meyer-Vernet & Sicardy, 1987; Pringle, 1991; Artymowicz & Lubow, 1994), binaries can exert strong torques on gas only a few binary separations away when that gas orbits in the same sense as the binary. This torque can be large enough to substantially affect the structure of the disk (as we have already seen in our discussion of the surface density profile). In addition, it can be large enough to significantly influence the long-term evolution of the binary orbit itself. However, because this torque can conveniently be described (in linear theory) as a sum over resonances, extrapolation from the linear regime suggests that the torque either does not exist at all or is much weaker in retrograde systems (Nixon et al., 2011a). Our simulation data can test this argument.

In Figure 3.7 we plot the mean local torque density $\mathcal{T}_z$ per unit mass:

$$\langle \mathcal{T}_z \rangle = \left(\frac{GMa}{2}\right) \int_t \frac{1}{T} \frac{\int_0^{2\pi} \Sigma_{(r,\phi)} \left[\frac{\sin(\phi_1 - \phi)}{R_1^3} + \frac{\sin(\phi_2 - \phi)}{R_2^3}\right] r \, d\phi}{\int_0^{2\pi} \Sigma_{(r,\phi)} \, d\phi} dt' \qquad (3.3)$$

Here $R_{1,2} = \left[\left(\frac{a}{2}\right)^2 + r^2 - a\, r \cos(\phi - \phi_{1,2})\right]^{1/2}$ are the distances between the disk mass element and the primary and secondary binary members, $\phi_{1,2}$ are the azimuthal angular positions of the primary and secondary binary members, and ϕ is the azimuthal position of the disk mass element. The duration T of time-averaging was $500 \leq t \leq 563$ in the retrograde case, and $400 \leq t \leq 463$ in the prograde case.

Viewed in this way, the two cases are dramatically different. The prograde case has a very large torque per unit mass in the gap region, indeed this large torque is why there is a gap. In notable contrast, there is no such feature in the retrograde case. Moreover, the magnitude of the torque per unit mass is $\sim 100\times$ greater in the prograde than in the retrograde case. Thus, as expected, flipping the sign of orbital motion in the disk has a drastic effect on the binary torque. These results are quantitatively similar to those reported by RS14 in the sense that there is very little angular momentum transferred gravitationally; the net angular momentum transport in the retrograde case is entirely associated with accretion.

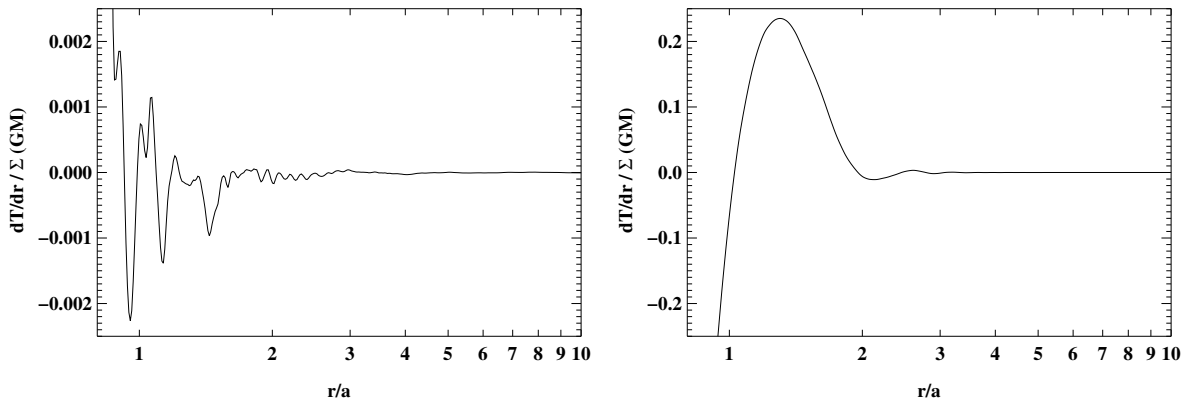

Figure 3.7: Time-averaged local gravitational torque per unit mass exerted by the binary on the circumbinary disk. Left: retrograde, averaged over the period $500 \leq t \leq 563$; right: prograde, averaged over $400 \leq t \leq 463$. Note that the vertical scale of the plot on the left is two orders of magnitude smaller than that of the plot on the right.

3.4 Interactions With Inner Accretion Disks

As our simulation demonstrated, retrograde circumbinary disks around an equal-mass circular-orbit binary extend at least as close in as $r \simeq a$. In addition, they are able to transfer to the binary essentially all the accretion passing through them from farther away. We therefore expect that each member of the binary possesses its own individual accretion disk. In a situation like this, tidal torques exerted on each disk by the other member of the binary limit their radial extent. A variety of estimates exist in the literature for the sizes of such disks. The calculations of Paczyński (1977) for circular orbits of various mass-ratios are well fit by the expression $r_* \simeq 0.27 q_*^{0.3} a$, where r is the radius of the disk around a member of the binary and q is the ratio of that object's mass to its companion's mass. Papaloizou & Pringle (1977) found roughly similar results, while Artymowicz & Lubow (1994), adopting a somewhat different formalism, found disk sizes in circular binaries differing by tens of percent from these earlier estimates and also estimated disk sizes in eccentric binaries, finding them to be generally rather smaller.

Despite these uncertainties, it nonetheless remains clear that interactions between the individual inner disks and a retrograde circumbinary disk are likely even when the binary orbit is nearly circular. In the limit of $q \ll 1$, in which the secondary would orbit at $r \simeq a$, any accretion disk around it would interact strongly with a retrograde circumbinary disk. It would be almost as likely in the opposite extreme of $q = 1$, in which both members orbit at $r = 0.5a$; if their disks extend out a distance $\simeq 0.3a$, they would graze against the inner edge of a circumbinary disk that reaches $r = 0.8a$. Such interactions are even more likely when the binary orbit is strongly eccentric and $q < 1$ (RS14).

If these disks do come into contact with each other, the fluid at the inner accretion disks' outer edges will shock against the fluid orbiting at the circumbinary accretion disk's inner edge, as orbital speeds in thin disks are always very high Mach number. To be more precise, a pair of shocks will form, a forward shock where the circumbinary disk gas is deflected toward joining the circulation around the inner disk, and a reverse shock where gas already orbiting within the inner disk is deflected by the pressure of the inter-shock region. In the usual fashion, a contact discontinuity separates the two post-shock regions.

It is easiest to analyze these shocks in the frame of the secondary. Although we have not directly demonstrated this, we assume that the inner disk rotates in the sense of the circumbinary disk, not the binary orbit. There are two principal reasons why we do so. Even for the secondary, the more rapidly moving member of the binary, the ratio of the orbital speed at the inner edge (radius r_d) in the circumbinary disk to the orbital speed of the secondary at apocenter is:

$$\frac{v_{\rm disk}}{v_{\rm orbit}} \;=\; (1+q)\,\sqrt{\frac{1+e}{1-e}\,\frac{a}{r_d}} \tag{3.4}$$

For $q = 1$ and $e = 0$ (the case treated in our simulation), this ratio is $2\sqrt{\frac{a}{r_d}}$. The ratio decreases when $q < 1$, but by at most a factor of 2, and increases when $e > 0$, but is always greater than or equal to $\sqrt{\frac{a}{r_d}}$. Thus, for most parameter combinations $v_{disk} > v_{orbit}$. In addition, orbital motion in the inner disk with this sense minimizes shear within the shocked circumbinary disk gas.

Although there are two shocks, with this sense of rotation for the gas around the secondary, the forward shock should be considerably stronger than the reverse shock. In our evaluation of the associated heating and radiation, we will therefore

focus on it. The magnitude of the shock speed at the forward shock is always of order $v_0 = v_{\rm disk} + v_{\rm orb}$ because the shock has this speed at the leading point on the outer edge of the inner disk, where the orbital velocity of gas around the secondary is perpendicular to the orbital velocity of the secondary itself. However, in general it is somewhat less than v_0 by a factor $\sin(\Psi)$, where Ψ is the angle between the shock front and the azimuthal direction. The post-shock temperature is then:

$$kT_{\rm s} = \left(\frac{3}{16}\right) \bar{m} \sin^2(\Psi)\ v_0^2 \tag{3.5}$$

We have assumed the gas's adiabatic index is $\frac{5}{3}$, $\bar{m}$ is the mean mass per particle, and the shock speed $v_s = \alpha v_0$. The global rate of heating due to the forward shock can then be easily estimated on the assumption that all matter flowing into the zone swept out by the secondary's disk is eventually shocked:

$$L_{\rm shock} = \left(\frac{9}{32}\right) \dot{M} \sin^2(\Psi)\ v_0^2 \tag{3.6}$$

So far in this discussion we have analyzed the situation as if the interaction were taking place for the first time, with the prior structure of both the inner disk and the circumbinary disk unaltered from what they would be in the absence of interactions. This is, of course, unrealistic. Nonetheless, it may not be such a bad approximation. Suppose, for example, that the result of the first such collision is to remove matter from both the outer edge of the inner disk and the inner edge of the outer disk. Subsequent material making its way inward through the circumbinary disk will eventually strike the inner disk with relative velocity $\sim v_0$ in any event, whether it is because

the circumbinary disk now extends sufficiently far inward, so that the shock has the form just envisioned, or because the material breaks away from the circumbinary disk and only then collides with the inner disk.

The ratio between this luminosity and the luminosity produced by accretion onto the black holes is $\sim \left(\frac{v_0}{c}\right)^2 \eta^{-1} \sim \left(\frac{R_g}{a(1+e)}\right)^2 \eta^{-1}$, where η is the radiative efficiency of the accretion onto the black holes. This ratio is $\lesssim 0.01$ until $a(1+e)$ becomes $\lesssim 1000\, R_g \left(\frac{\eta}{0.1}\right)^{-1}$. However, even when $a(1+e) \gtrsim 1000\, R_g$, it may be discernible in other ways. In particular, if the binary is eccentric, the heating rate is strongly modulated on the binary orbital period. Provided the cooling time from the post-shock region is shorter than or comparable to the binary period, the emergent luminosity will be similarly modulated.

Once $a(1+e)$ does become $\lesssim 1000\, R_g$, it is possible for the luminosity in these shocks to be great enough to stand out against conventional active galactic nucleus (AGN) emission generated by the individual black hole disks. When the potential is this deep, the shock speed is great enough to make the shocks' structure and radiative properties resemble those predicted to exist in prograde systems by Roedig et al. (2014), where it was argued that most of the luminosity should emerge in hard X-rays, $\sim$100 keV. Because in typical AGN, hard X-rays account for only a fraction $\sim$0.2 of the bolometric luminosity, and the temperature expected in these shocks might actually exceed that characteristic of the ordinary coronal hard X-rays because there are fewer local seed photons, the shock component might be apparent even for $a(1+e)$ as large as $\sim 1000\, R_g$.

However, the existence of a strong shock at the inner edge of the circumbinary disk depends on the ability of that inner edge to track the evolution of $a(1+e)$. Ultimately, the rate of orbital evolution by gravitational wave emission becomes larger

than the inflow rate within the disk (Milosavljević & Phinney, 2005); from that point onward, the bulk of the disk is left at larger radius than the binary apocenter. If the inflow rate is estimated via the α_{SS} model, the criterion for this decoupling time is a function of the disk thickness as well as binary semi-major axis: $H/R \gtrsim 10q^{1/2}(1+q)^{1/4}(R_g/a)^2(0.1/\alpha)^{1/2}(R/R_g)^{3/4}$

In this context, however, it is also worth pointing out that, at least until decoupling, the "notch" predicted by Roedig et al. (2014) should not be significant in the spectra of retrograde systems, precisely because the streams leaving the inner edge of the circumbinary disk cross such a narrow range in radius before striking the outer edge of an inner accretion disk.

3.5 Binary Evolution

The size and shape of a binary's orbit are characterized by its semi-major axis (a) and orbital eccentricity (e). An investigation into the evolution of these parameters begins with the most fundamental quantities of orbital mechanics (total energy and angular momentum). The total energy of a bound, gravitational binary orbit is given by:

$$E = -\frac{G\,M_1\,M_2}{2\,a} = -\frac{q}{(1+q)^2}\frac{GM^2}{2a} \tag{3.7}$$

Here G is the Newtonian gravitational constant, M = M_1+M_2 is the total mass of the binary, and q = $\frac{M_2}{M_1} \leq 1$ is the binary's mass ratio. The total angular momentum of the binary's orbit is:

$$J \;=\; \frac{q}{(1+q)^2}\,\sqrt{G\,M^3\,a\,(1-e^2)} \tag{3.8}$$

From these two physical quantities, we extract expressions for the orbital semi-major axis:

$$a \;=\; -\,\frac{q}{(1+q)^2}\,\frac{G\,M^2}{2\,E} \tag{3.9}$$

and eccentricity:

$$e \;=\; \sqrt{1+\frac{2\,(1+q)^6\;E\,J^2}{G^2\,M^5\,q^3}} \tag{3.10}$$

It follows that the time derivatives of these parameters are:

$$\frac{\dot{a}}{a} \;=\; 2\,\frac{\dot{M}}{M}-\frac{\dot{E}}{E}+\frac{1-q}{1+q}\,\frac{\dot{q}}{q} \quad , \quad \dot{e} \;=\; \frac{1-e^2}{2e}\left[5\,\frac{\dot{M}}{M}-2\,\frac{\dot{J}}{J}-\frac{\dot{E}}{E}+3\,\frac{1-q}{1+q}\,\frac{\dot{q}}{q}\right] \tag{3.11}$$

Note that the term $\propto \dot{q}/q$ in both orbital evolution equations was omitted in the treatment of this problem by Nixon et al. (2011a).

Although these expressions display $\frac{\dot{E}}{E}$, $\frac{\dot{q}}{q}$, and $\frac{\dot{J}}{J}$ as quantities independent of $\frac{\dot{M}}{M}$, in fact all three of the former group should be $\propto \dot{M}/M$ because, in the absence of binary-disk torques, the way energy, mass, and angular momentum are delivered to the binary is through accretion. Thus, the problem reduces to determining the

proportionality relations.

Only $(\frac{\dot{J}/J}{\dot{M}/M})$ can be determined reliably from our simulation data. As remarked above, $\frac{\dot{J}}{\dot{M}} \simeq -1.25$ in our simulation, in which $q = 1$ and $e = 0$. Note that there is a suppressed unit of GMa implied. Because the interaction between an eccentric binary and the inner edge of a circumbinary disk is most likely to occur near apocenter, we expect that $\frac{\dot{J}}{\dot{M}} \propto \sqrt{1+e}$ for fixed a and q. To lowest-order, $\frac{\dot{J}}{\dot{M}}$ should be independent of q because the specific angular momentum of the accreting material is not very different from what it had while orbiting at the inner edge of the circumbinary disk, and it does not matter which of the binary's members captures the matter for the binary to absorb that angular momentum. However, there may be a weak dependence on q associated with binary torques acting on the streams in the time between their departure from the disk and their capture by the binary.

The ratio $\frac{\dot{q}/q}{\dot{M}/M}$ depends, of course, on the fraction of the accretion flow reaching each member of the binary, but our inner cut-out prevents us from measuring that. Most studies investigating this question (e.g., Artymowicz & Lubow (1996); Nixon et al. (2011a); Farris et al. (2014) ; RS14; Shi & Krolik (2015)) have suggested that the majority of the accretion flow goes to the secondary, so that $\dot{q}$ is always positive; indeed, for the purpose of predicting orbital evolution under these circumstances, several of these authors have assumed that essentially all the accretion flow goes to the secondary. However, there is as yet little information about how $\dot{q}$ depends on q or e. We therefore parameterize our ignorance in terms of the fractions f_1 and f_2 going, respectively, to the primary and the secondary; we require that $f_1 + f_2 = 1$. With this parameterization,

$$\dot{q} \;=\; (1+q)(f_2 - q\, f_1)\frac{\dot{M}}{M} \tag{3.12}$$

from which we may infer that $\dot{q} > 0$ and $|\dot{q}| \simeq \frac{\dot{M}}{M}$, except when $q \simeq 1$.

The rate of energy loss is the most uncertain. A variety of models have been constructed to estimate it (see, e.g., Nixon et al. (2011a)). For our present purposes, we remark only that dissipative losses should make $\dot{E} < 0$ and we might reasonably expect that $\frac{\dot{E}}{E} \sim \frac{\dot{M}}{M}$. A more detailed discussion of this relationship is given in Schnittman & Krolik (2015), where it is found that this quantity's dependence on q and e is somewhat complicated, but the sign of $\frac{\dot{E}}{E}$ is always positive, i.e., orbital energy is consistently lost.

Combining these estimates, we find that $\dot{e}/\frac{\dot{M}}{M}$ should be consistently positive, as the angular momentum, mass, and mass ratio terms in Equation 3.11 are all positive. As argued in Schnittman & Krolik (2015), its value is generally ~ 10 until e approaches unity.

A general treatment of $\dot{a}$ is complex, but given two reasonable assumptions, the evolution of the semimajor axis may be easily determined in terms of $\dot{e}$. If the accretion predominantly takes place at the apocenter and the accretion stream travels tangentially to the orbit immediately before it is captured, $a(1+e)$ should be nearly constant. Because e can change only from 0 to 1, a can decrease by at most about a factor of 2.

On the other hand, the strong growth of eccentricity can cause $a(1-e)$ to shrink by a much larger factor, as already concluded by Nixon et al. (2011a). When the members of the binary are main sequence stars or white dwarfs, the continued diminution of the pericenter distance must result in a direct interaction between the two stars through mass transfer or merger. When the members of the binary are either black holes or neutron stars, $a(1-e)$ can become small enough for gravitational wave losses to

become important to the further evolution of the system. For a detailed analysis of these effects and a more specific estimate of $\frac{\dot{E}}{E}$ appropriate to these circumstances, see the companion paper Schnittman & Krolik (2015).

In sum, for as long as $1 - e$ is not $\ll 1$, the rate of evolution of a retrograde binary's semi-major axis $\frac{\dot{a}}{a} \sim -10\frac{\dot{M}}{M}$. This is an order of magnitude larger than the rate of orbital evolution found for prograde disks: for example, the data of SK12 imply $\frac{\dot{a}}{a} \simeq -0.8\,\frac{\dot{M}}{M}$. However, it is possible that the typical $\frac{\dot{a}}{a}$ magnitude for prograde cases is actually rather larger than found in SK12. In the particular case studied by SK12, the binary angular momentum lost to binary-on-disk torques and gained by accretion (both of magnitude $\sim 5\frac{\dot{M}}{M}$) nearly canceled each other, leaving the net rate nearly a factor of 10 smaller than the magnitude of either rate individually, a cancellation whose precise value is very likely to be sensitive to particular parameter choices. Less complete cancelation might increase the ratio $(\frac{\dot{a}}{a})/(\frac{\dot{M}}{M})$ by a factor of several. Thus, binaries surrounded by retrograde circumbinary disks evolve (both decreasing semi-major axis and increasing orbital eccentricity) at a rate much larger than those with prograde circumbinary disks.

Chapter 4 Eccentric Binaries

In this study we investigate prograde circumbinary accretion disks surrounding equal mass binaries on eccentric orbits. Our goals for this investigation are two fold. First we seek to understand the evolution of the binary's orbital characteristics (semi-major axis a and eccentricity e). Binary evolution has implications across a wide range of mass scales, from planetary formation in protostellar systems to the effect of SMBHBs on galactic dynamics. Second, we explore the orbital phase dependence of mass accretion, binary torque, binary angular momentum evolution, and binary energy evolution to gain a better understanding of the nature of accretion onto eccentric binaries. Periodicity of mass accretion onto binaries has been noted by others (e.g. MacFadyen & Milosavljević (2008), SK12, Farris et al. (2014); Miranda et al. (2016)), however, we believe that we are the first to do a detailed investigation into the orbital phase dependence of the aforementioned quantities for eccentric binaries.

We evolved the circumbinary disks for ~ 440 simulation time units (~ 70 binary orbits) to allow them to enter a quasi-steady state. We say quasi-steady state because while the eccentric orbit of the binary caused moderate, periodic motion of the material at small radii ($r \leq 2a$), Figure 4.1 shows that the large-scale mass distribution remained unchanged over the span of the analysis period. The outer disk ($r \geq 10a$), however, do not achieve such an equilibrium as these regions continued to expand outwards while receiving angular momentum from the inner regions of the disk.

We perform our analysis over a time span beginning at simulation time 400 and extending for six binary orbits (Hereafter referred to as the analysis period). We use six binary orbits in order to have enough data for time averaging and to observe phase dependent behavior. We use the following terminology to simplify our descriptions of the phase dependence of computed quantities. We refer to the portion of the binary orbit during which the binary transitions from periapsis towards apoapsis as the binary's ascent phase and the portion of the binary's orbit during which the binary transitions from apoapsis toward periapsis as the binary's descent phase.

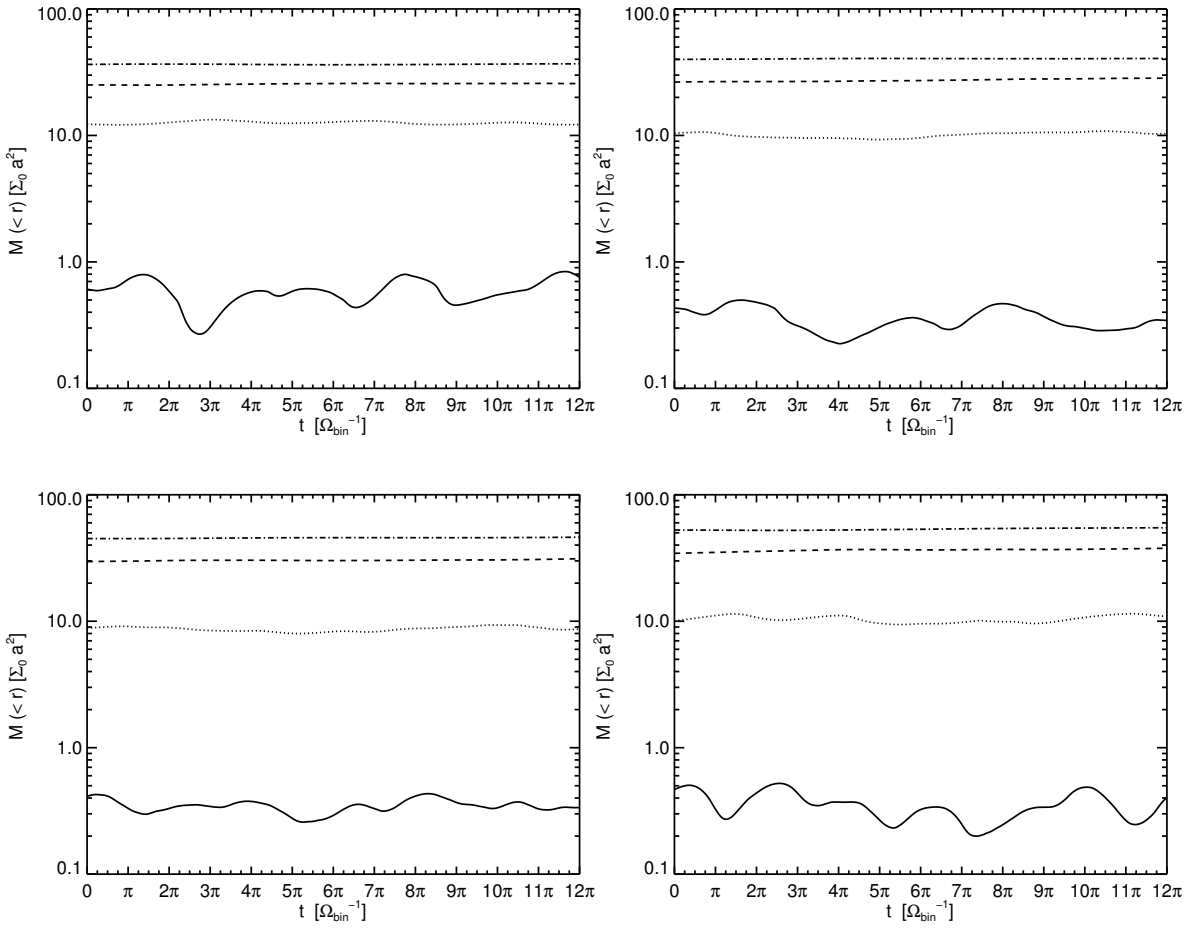

Figure 4.1: Disk mass profile history during the analysis period. The disk mass within r = 2a is shown by the solid curve, 3a the dotted curve, 4a the dashed curve, and 5a the dot-dashed curve. Top Left: e = 0.2, Top Right: e = 0.4, Bottom Left: e = 0.6, Bottom Right: e = 0.8.

4.1 Density Profile

Figure 4.2 shows vertically integrated surface density snapshots from simulation times (438, 442, 443, 437) for eccentricities (0.2, 0.4, 0.6, 0.8) respectively. These plots illustrate the accretion streams passing into the binary region. Note also the continuity between the accretion streams and the spiral density waves in the disk.

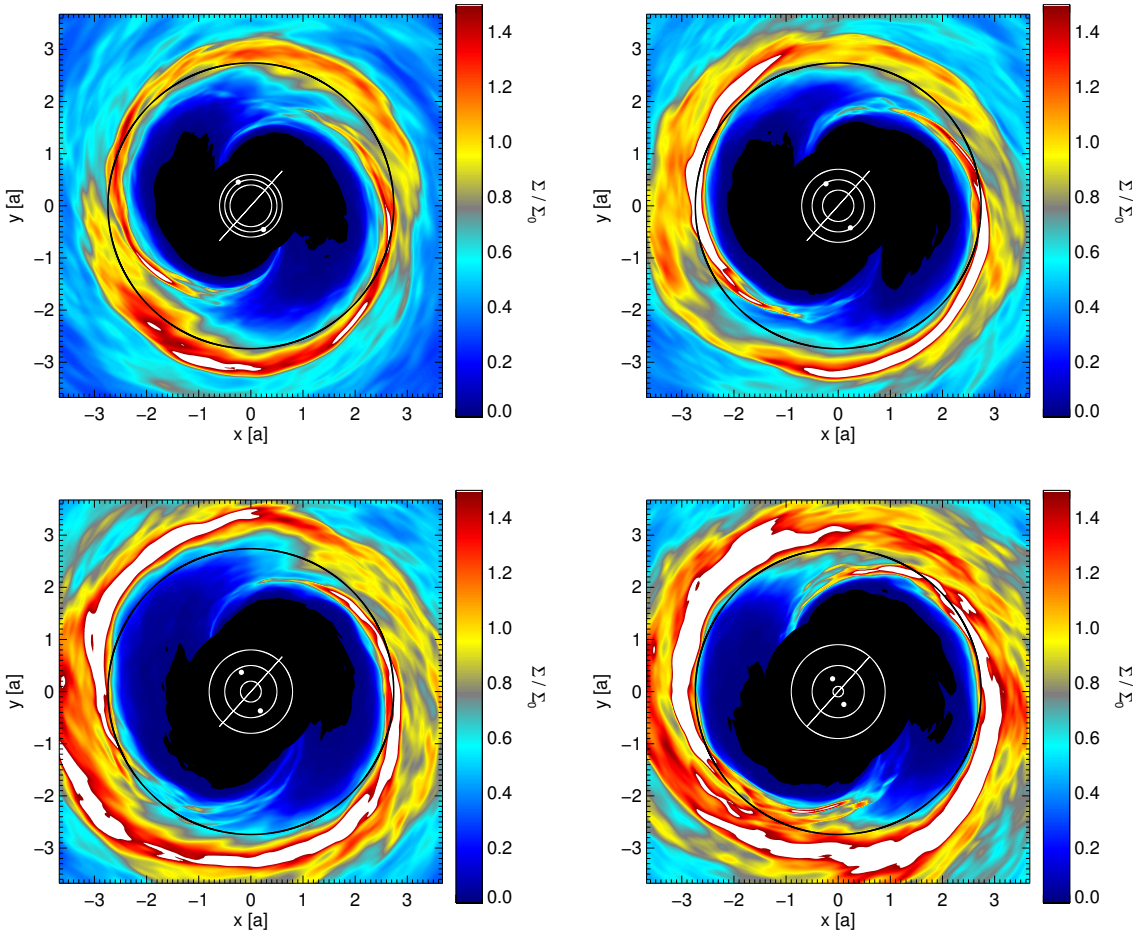

Figure 4.2: Vertically integrated surface density in prograde circumbinary accretion disks. These images highlight the accretion streams which feed gas through the gap region and into the binary region. Top Left: e = 0.2, Top Right: e = 0.4, Bottom Left: e = 0.6, Bottom Right: e = 0.8. The inner white ring denotes the minimum binary orbital radius. The middle white ring has a diameter equal to the semi-major axis of the binary orbit. The outer white ring denotes the maximum binary orbital radius. The solid black ring which can be seen inside the circumbinary disk itself denotes the position of the shell and time averaged maximum of the disk surface density. The solid white line indicates the orientation of the binary at periapsis and apoapsis.

In Figure 4.3 we show the shell and time-averaged surface density profiles for each disk. Strong binary-induced torques prevent the disk material from accreting directly into the binary region, creating a gap between the binary and the main body of the circumbinary disk. As matter spreads out from the initial axisymmetric torus used as the initial condition in SK12, it piles up at the outer boundary of this gap region creating peaks in the surface density. Given a long enough time, the excess surface density would accrete into the binary leaving a smoother density profile. For our purposes, this peak in the surface density is a good indicator of the extent of the gap region. We found that the surface density peak value increases monotonically with eccentricity. The location of the peak surface density, however, seems to asymptotically approach $r = 3.2a$ as eccentricity approaches 1.

Our simulations use the data produced by SK12 as our initial conditions, branching off before the development of the non-axisymmetric "lump". However, we do not include the $e = 0$ data from SK12 in Figure 4.3 . The reason for this is that in making the transition between the circular and eccentric binary simulations, there was a change of coordinates to accomodate the growth in the binary orbit. The inner edge of the computational boundary was pushed outward and the grid cells were recalculated to maintain the same grid scheme. This lead the mass distribution in the disk to rearrange itself to accommodate the new grid cells as well as the new gravitational potential. This had the effect of increasing the surface density peak at small radii and smoothing out the density profile at larger radii. Since, each of the eccentric binary simulations underwent a very similar process, it is acceptable to compare them with each other, but comparisons with the $e = 0$ surface density distribution is less appropriate.

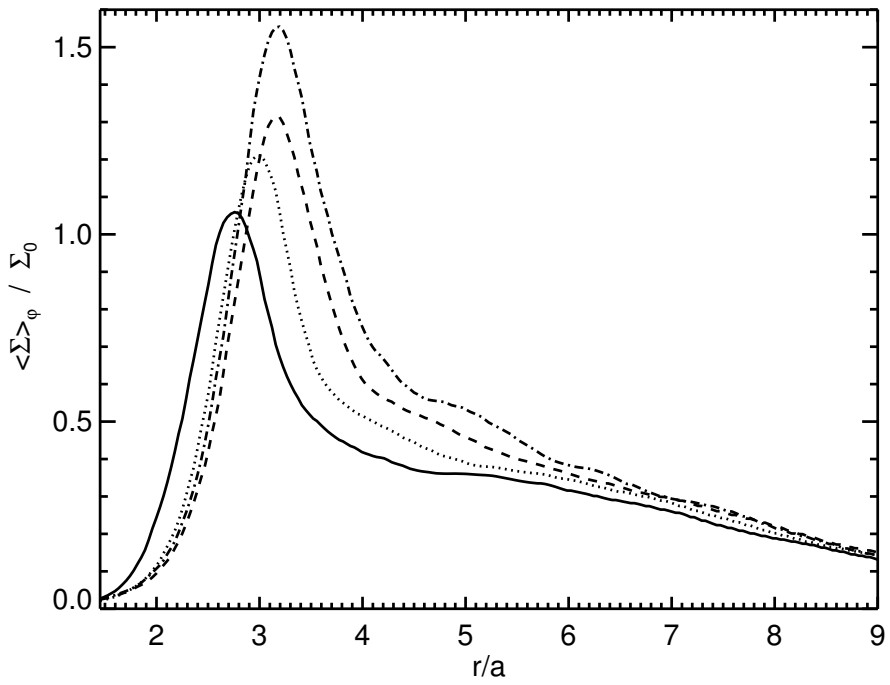

Figure 4.3: Time and shell integrated surface density. Time averaged over the analysis period. Solid: e = 0.2, Dotted: e = 0.4, Dashed: e = 0.6, Dot-Dashed: e = 0.8. The peak surface density values (1.07, 1.22, 1.31, 1.54) [Σ_0] occur at radii (2.83, 3.05, 3.18, 3.18) [a] for eccentricities (0.2, 0.4, 0.6, 0.8) respectively.

For Figure 4.4 , we computed the Fourier transform of the azimuthal oscillations of the integrated surface density. We averaged the Fourier coefficients of the azimuthal spectra from $r = 2a$ to $r = 4a$ and time averaged them across the extent of the analysis period. These plots indicate that the dominant surface density feature is an m = 2 azimuthal density oscillation. This is different than what has been found for circular orbit binaries. SK12 found a pronounced $m = 1$ azimuthal density oscillation which they referred to as a "lump". The details of the $m = 1$ density feature in prograde circumbinary disks surrounding circular orbit binaries and its formation are discussed in SK12 and SK15. MacFadyen & Milosavljević (2008) explain that the m = 2 spiral density waves are created as the binary exerts strong torques on the

disk material at the inner edge of the main body of the disk. The imparted angular momentum propagates through the disk body creating the spiral features. These strong torques occur at the position of the m = 2 outer Lindblad resonance ($r \simeq 2a$) (Nixon & Lubow, 2015). This location corresponds roughly to the inner edge of the main disk. While each binary had a dominant feature at m = 2, we did not find any trend in the power spectra with respect to binary eccentricity.

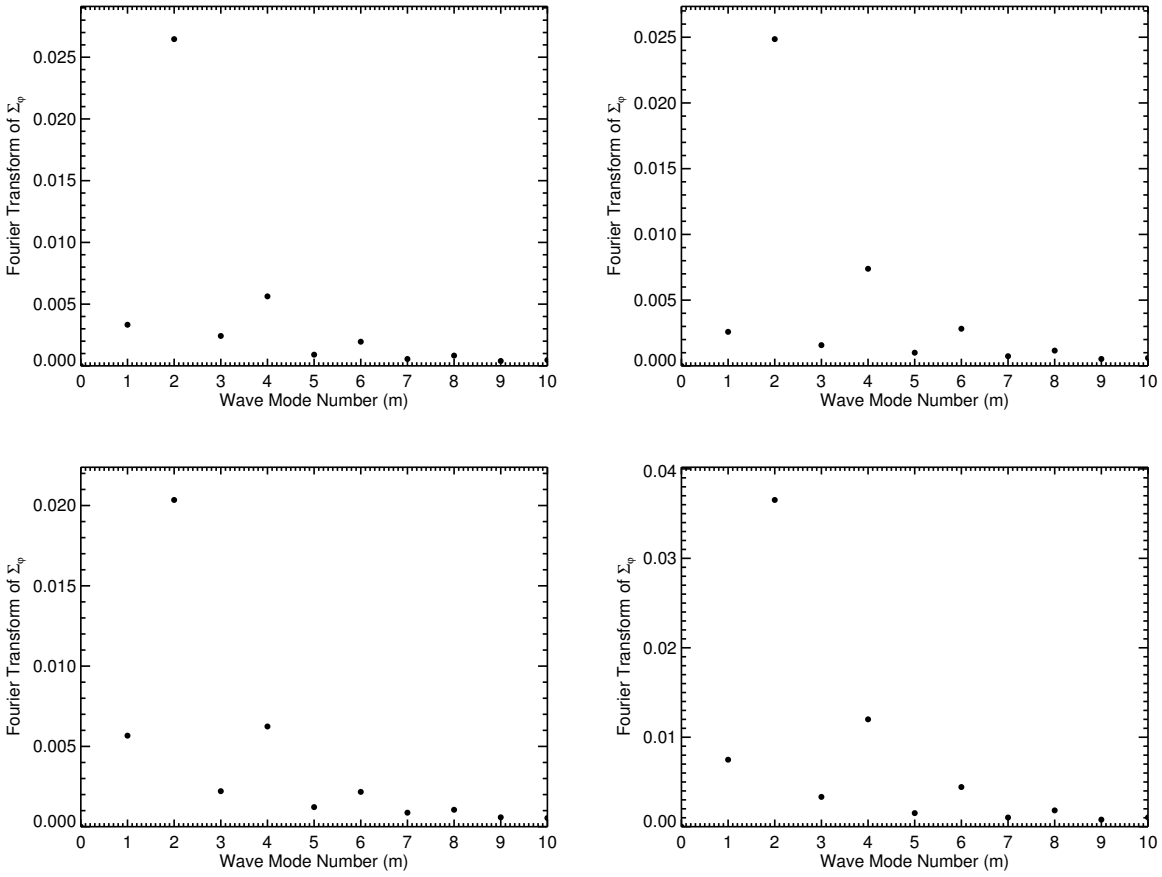

Figure 4.4: Fourier transform of azimuthal density oscillations. Averaged from $r = 2a$ to $r = 4a$ and time averaged over the analysis period. Top Left: e = 0.2, Top Right: e = 0.4, Bottom Left: e = 0.6, Bottom Right: e = 0.8.

4.2 Mass Accretion

Unlike retrograde circumbinary disks, prograde circumbinary disks cannot accrete directly into the binary region. Positive binary-on-disk torques create a gap between the binary and the accretion disk main body. Mass accretion occurs when attractive gravitational torques strip angular momentum from streams of material allowing them to cross the gap region. As material from the streams passes into the binary region, the accretion rate peaks. After a short time (less than a binary orbit) positive gravitational torques inject angular momentum into the accretion streams causing the unaccreted material to move back out into the gap region resulting in a decline in the mass accretion rate. We discuss these torques in greater detail in a later section.

The mass accretion rate ($\frac{\dot{M}}{M}$) through the inner computational boundary, time averaged over the analysis period, is (0.019, 0.029, 0.046, 0.054) $\left[\Omega_{bin} \frac{\Sigma_0 a^2}{M}\right]$ for eccentricities (0.2, 0.4, 0.6, 0.8) respectively. These time averages suggest that the mass accretion rate increases with binary orbital eccentricity. It is useful to convert these results into relatable values. We define $M' \equiv \frac{M_{bin}}{M_\odot}$, $a' = \frac{\text{s.m. axis}}{0.1\text{pc}}$, and $\gamma = \frac{\Sigma_0 a^2}{M}$. As a fraction of the inverse Salpeter time (radiative efficieny $\eta = 0.1$) our accretion rates are: $\frac{\dot{M}}{\dot{M}_{Edd}} = (1.8, 2.7, 4.5, 5.0)\ [\gamma\ (M')^{3/2}\ (a')^{-5/2}]$ for eccentricities (0.2, 0.4, 0.6, 0.8) respectively.

In Figure 4.5 we present the shell integrated mass accretion rate through the inner edge of the computational zone for each eccentricity as a function of simulation time. These plots show a periodicity in the mass accretion rate, a trend which weakens as binary orbital eccentricity approaches 1. Accretion periodicity at the frequency of the binary orbit has been noted by others (e.g. Artymowicz & Lubow (1996); MacFadyen & Milosavljević (2008); SK12; Farris et al. (2014); Miranda et al. (2016))

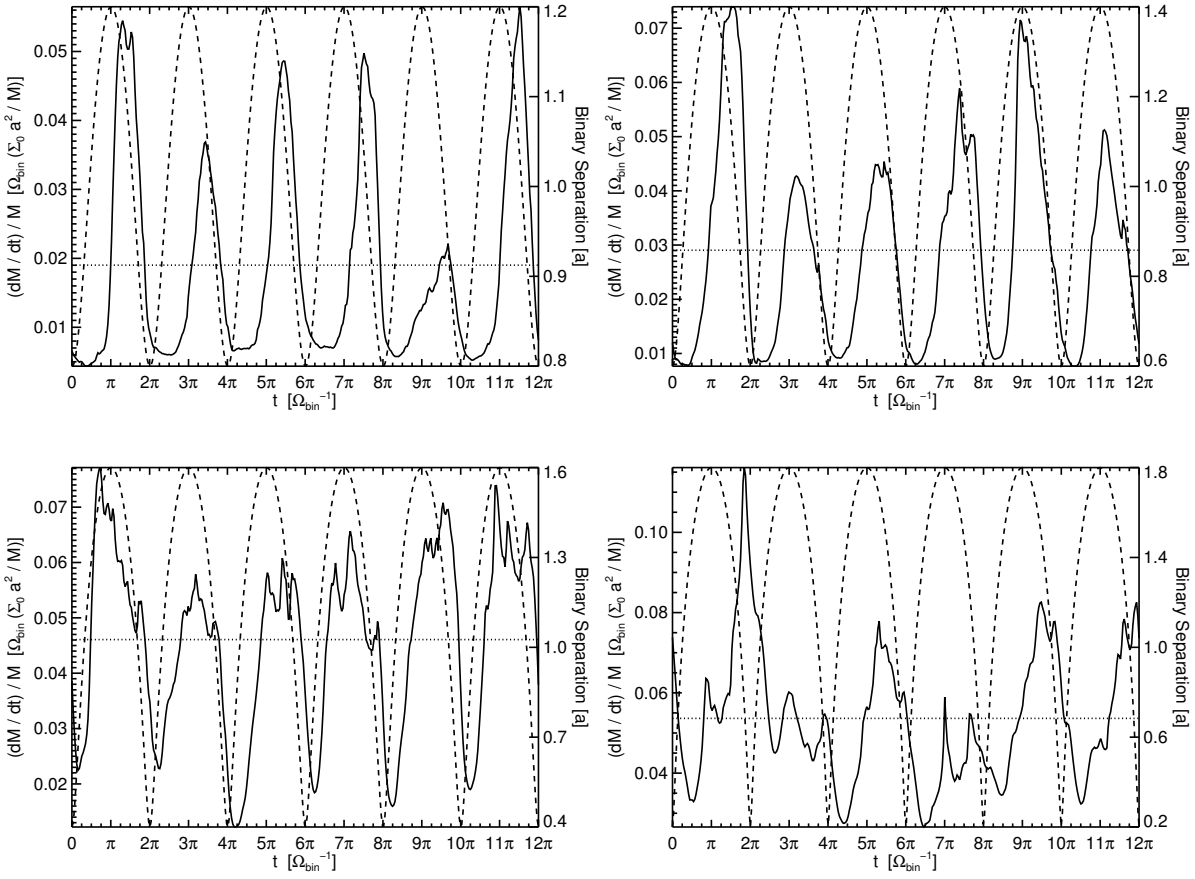

Figure 4.5: Accretion rate through the inner boundary as a function of simulation time during the analysis period. Top Left: e = 0.2, Top Right: e = 0.4, Bottom Left: e = 0.6, Bottom Right: e = 0.8. The dotted lines in each graph indicate the time-averaged value. The dashed curve shows the binary separation as the binary moves from periapsis to apoapsis and back. Note that the scales for $\frac{\dot{M}}{M}$ and binary separation change for each graph.

To better understand the phase dependence, we show the accretion rate data re-binned into a single binary orbit in Figure 4.6 . These plots focus on the manner in which the accretion rate evolves throughout the binary orbit. For all binary eccentricities, the peak in the mass accretion rate occurs during the binary's descent phase, and for most binary eccentricities ($e = 0.8$ is the exception) near apoapsis. As the binary eccentricity increases, the accretion rate remains high for a larger fraction of the binary orbit because large eccentricity binaries do not produce strong enough

positive torques during the descent phase to fully propel the accretion streams out into the gap region. The reason that the positive torques are more pronounced for small eccentricity binaries is that, for smaller eccentricity binaries, the binary separation is still large ($\geq a$) as the accretion streams pass from negative to positive torque regions. Thus the distance between the binary and the disk material is smaller and the torque magnitudes are larger.

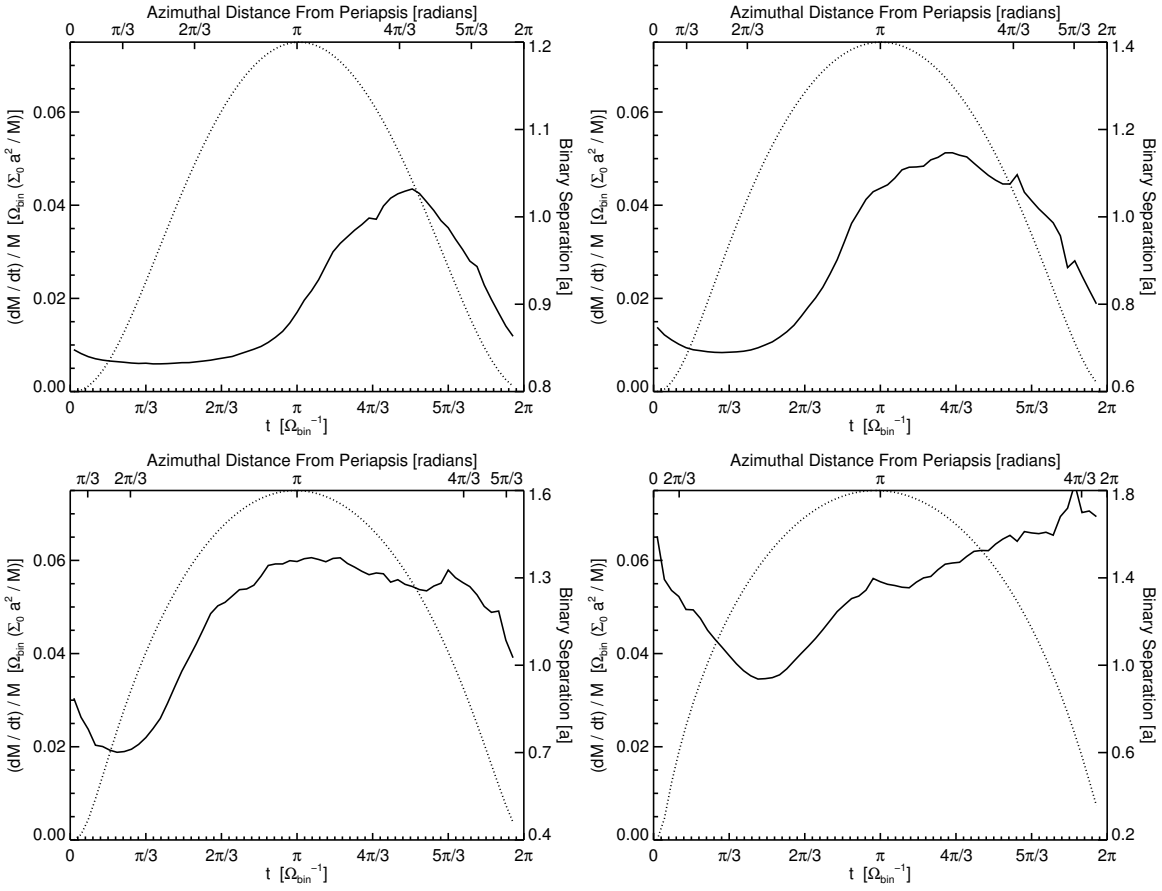

Figure 4.6: Accretion rate through the inner boundary as a function of simulation time, rebinned into a single binary orbit. The adjusted data points are the bin averages of the simulation data during the analysis period. The jagged sections are caused by bins with too few data points to create a smooth average. Top Left: e = 0.2, Top Right: e = 0.4, Bottom Left: e = 0.6, Bottom Right: e = 0.8. The dotted curve shows the binary separation as the binary moves from periapsis to apoapsis and back. The axis on top of the plots displays the binary's angular position relative to periapsis. Note that the scales for binary separation and azimuthal position change for each graph.

An eccentric binary spends the majority of its orbital period at separations larger than the semi-major axis. Even though the mass accretion rate may peak, for large binary eccentricities, when the binary separation is smaller than the semi-major axis, this does not automatically mean that most mass accretion into the binary region occurs during this portion of the orbit. In Figure 4.7 we show $\frac{dM}{d\phi}\frac{1}{M}$ with respect to binary azimuthal angular position. By integrating the mass accreted per unit angle, we find that the majority of mass is accreted when the binary separation is larger than the semi-major axis. Specifically, the fraction of accreted matter for $s > a$ is (0.63, 0.75, 0.78, 0.74) for eccentricities (0.2, 0.4, 0.6, 0.8).

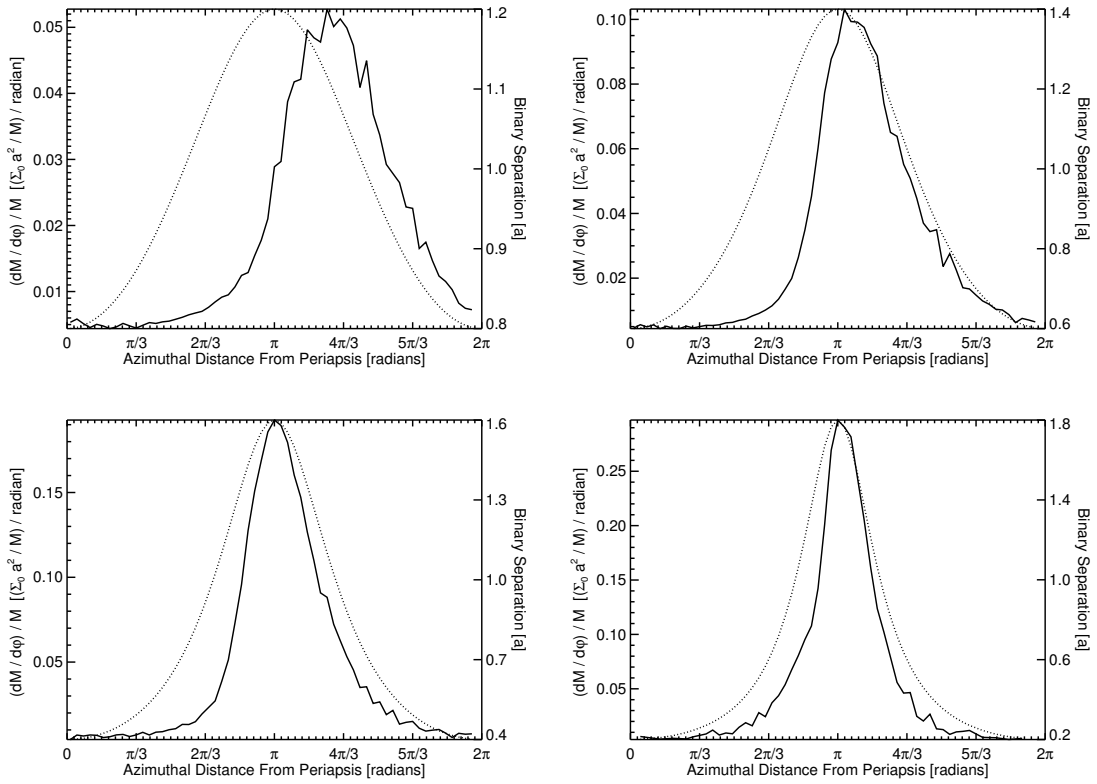

Figure 4.7: $\frac{dM}{d\phi}\frac{1}{M}$ through the inner boundary as a function of the binary azimuthal position, rebinned into a single binary orbit. The adjusted data points are the bin average of the simulation data during the analysis period. The jagged sections are caused by bins with too few data points to create a smooth average. Top Left: e = 0.2, Top Right: e = 0.4, Bottom Left: e = 0.6, Bottom Right: e = 0.8. The dotted curve shows the binary separation as the binary moves from periapsis to apoapsis and back. Note that the scales for $\frac{dM}{d\phi}\frac{1}{M}$ and binary separation change for each graph.

4.3 Binary Angular Momentum Evolution

A prograde circumbinary disk adds angular momentum to its central binary through accretion and removes it through gravitational torques. The net effect found in some previous studies of circular binaries is for the binary to gain angular momentum, though not specific angular momentum, over time (SK12, RS14). Other studies, however, have found a net loss of binary angular momentum over time (MacFadyen & Milosavljević, 2008; Rafikov, 2016). The time rate of change of the binary's angular momentum is $\dot{J} = \dot{M}\, j_{in} - T$. Here j_{in} is the specific angular momentum of the gas orbiting at the inner edge of the circumbinary disk, which we obtain from the simulation data. $\dot{M}\, j_{in}$ is thus the rate of angular momentum accretion into the binary region. T is the total binary-on-disk torque. In this section, we discuss the total angular momentum evolution of the binary and its constituent parts.

4.3.1 Binary-Disk Torques

In our analysis, we use the definition of the total binary-on-disk torque given in (MacFadyen & Milosavljević, 2008)

$$\frac{dT}{dr}_{(r)} \equiv -\int_0^{2\pi} \Sigma_{(r,\phi)} \frac{d\Phi}{d\phi}\, r d\phi \quad , \quad T \equiv \int_{r_{in}}^{\infty} \frac{dT}{dr'}_{(r')}\, dr' \tag{4.1}$$

In the gravitational potential (Φ) of an eccentric binary, the torque per unit area on a fluid element in the disk midplane ($-\Sigma_{(r,\phi)}\, \frac{d\Phi}{d\phi}$) is given by:

$$\tau = \frac{1}{4} G\, M\, \Sigma_{(r,\phi)}\, s\, r \left[\frac{\sin(\phi_1 - \phi)}{r_1^3} + \frac{\sin(\phi_2 - \phi)}{r_2^3}\right] \tag{4.2}$$

In both of these equations, $\Sigma_{(r,\phi)}$ is the vertically integrated, instantaneous surface density. In the second equation, s is the binary separation distance, and ϕ_i is the azimuthal position of the ith binary member. Positive values of the total binary-on-disk torque (T) denote that, the binary is losing angular momentum by depositing it via gravitational torques onto the circumbinary disk. Averaged over the analysis period, we find a monotonic increase in the total binary-on-disk torque T: (0.022, 0.024, 0.031, 0.39) $[GMa\Sigma_0]$ as well as the ratio of the total torque to the binary angular momentum $\frac{T}{J_{bin}}$: (0.091, 0.10, 0.15, 0.26) $\left[\Omega_{bin}\frac{\Sigma_0\, a^2}{M}\right]$ with increasing eccentricity (0.2, 0.4, 0.6, 0.8) respectively. Thus, on average, larger eccentricity binaries are better able to shed angular momentum via binary-on-disk torques. While this is an interesting result, it does not immediately translate into a statement on binary evolution. We discuss our work on binary evolution in a later section.

To explore the accretion streams in more detail, we look to the binary torque in the disk mid-plane. The disk plane is divided into quadrants of alternating positive and negative binary-on-disk torque. Positive torque regions are behind the nearer binary member's azimuthal position, negative ahead. Positive torque adds angular momentum to the disk material, causing it to move to larger radii. Negative torque removes angular momentum from the disk materal, causing it to move to smaller radii. In Figure 4.8 (Taken at identical times to Figure 4.2 near phase angle $\phi = \frac{5\pi}{3}$) we show a visual representation of these quadrants. Accretion streams form in the negative torque quadrants as material in the gap region and circumbinary's inner edge loses angular momentum. Specifically, they form when the binary is near apoapsis and the torque magnitudes are largest. These accretion streams take a fraction of a binary orbit to travel from the disk's inner edge to $r \sim a$ and reach the binary

region during the binary's descent phase (Artymowicz & Lubow, 1996). Figure 4.8 also shows that the accretion streams crossing the gap experience greater binary-on-disk torque than do any regions within the main disk. Finally, the plots show that the stream-repelling positive torques diminish in magnitude as eccentricity increases. This is consistent with our findings in the section on mass accretion rates.

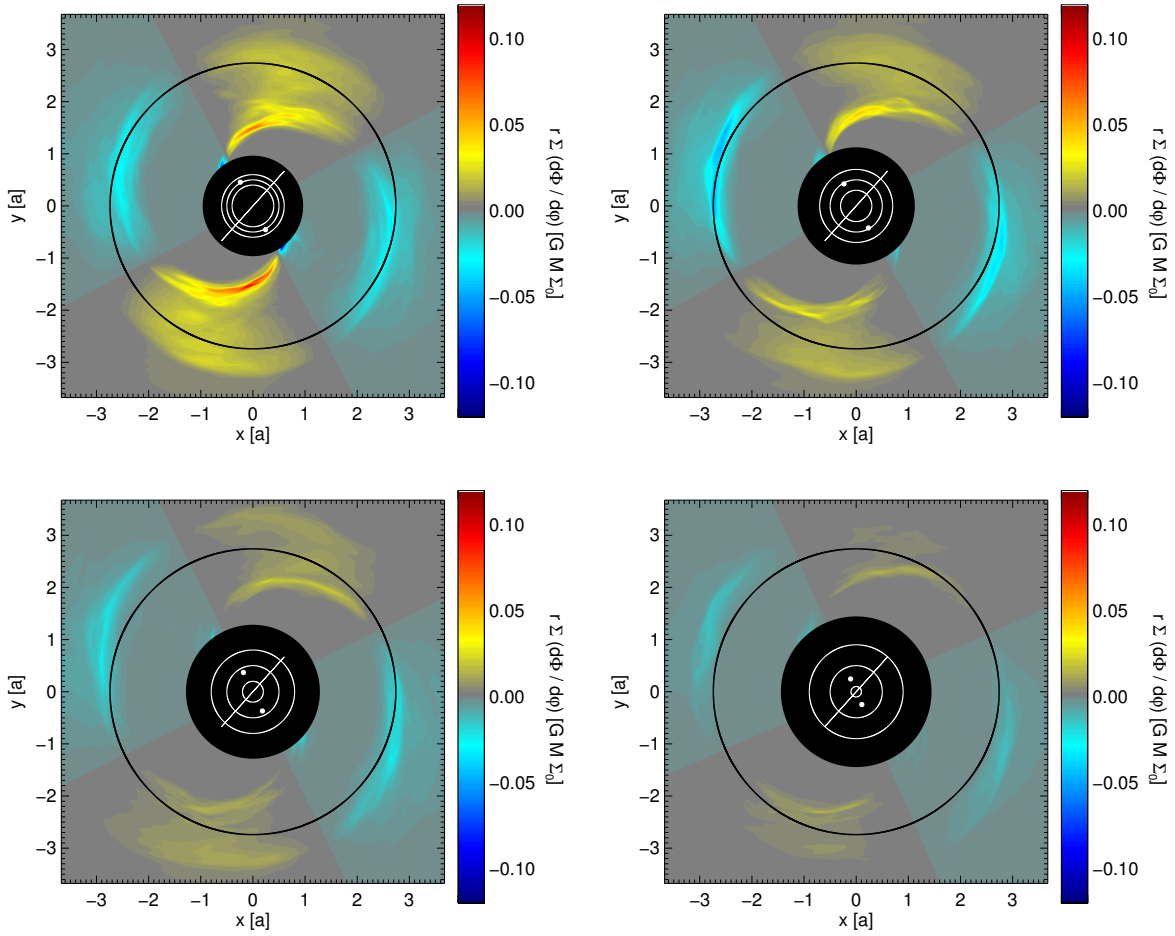

Figure 4.8: $\frac{dT}{dr}$ in the plane of the circumbinary disk. These images highlight the torque on the accretion streams which form during the descent phase of the binary orbit. Top Left: e = 0.2, Top Right: e = 0.4, Bottom Left: e = 0.6, Bottom Right: e = 0.8. The inner white ring denotes the minimum binary orbital radius. The middle white ring has a diameter equal to the semi-major axis of the binary orbit. The outer white ring denotes the maximum binary orbital radius. The solid black ring which can be seen inside the disks themselves denotes the position of the shell and time averaged maximum of the disk surface density. The solid white line indicates the orientation of the binary at periapsis and apoapsis. In the images and the color scale, blue tones indicate negative torque while yellow and red tones indicate positive torque.

Figure 4.9 shows the azimuthally averaged radial gradient of the binary-on-disk torque ($\frac{dT}{dr}$) as a function of radius, averaged over the analysis period. As seen by SK12 and Tang et al. (2017), at small radii ($r \lesssim a$) values are negative because the tips of the accretion streams pass into the binary region through negative torque quadrants. The gap region around the binary is formed as a result of the primary peak in the radial torque. The negative torque minima near $r = 3a$ corresponds to location of the peak density seen in Figure 4.3 . At larger radii, the azimuthally averaged radial torque gradient decays toward zero.

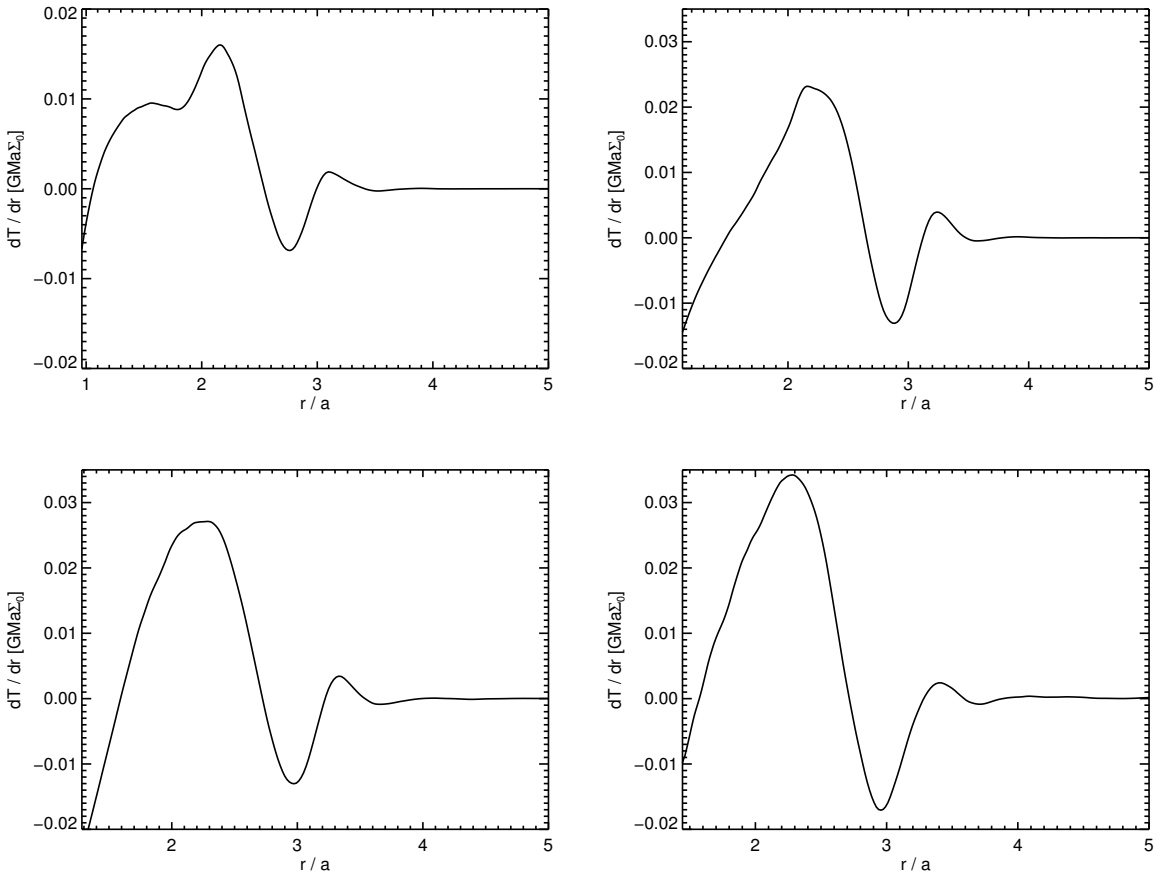

Figure 4.9: Azimuthally averaged radial binary-on-disk torque gradient ($\frac{dT}{dr}$) as a function of radius, averaged over the analysis period. Top Left: e = 0.2, Top Right: e = 0.4, Bottom Left: e = 0.6, Bottom Right: e = 0.8.

Figure 4.10 shows the ratio of the total binary-on-disk torque to the binary orbital angular momentum rebinned into a single binary orbit. The peak in the binary-on-disk torque occurs near apoapsis for all orbital eccentricities because the distance between the binary and the disk material is smallest here. Note that the peak moves from slightly after apocenter to somewhat before as eccentricity increases.

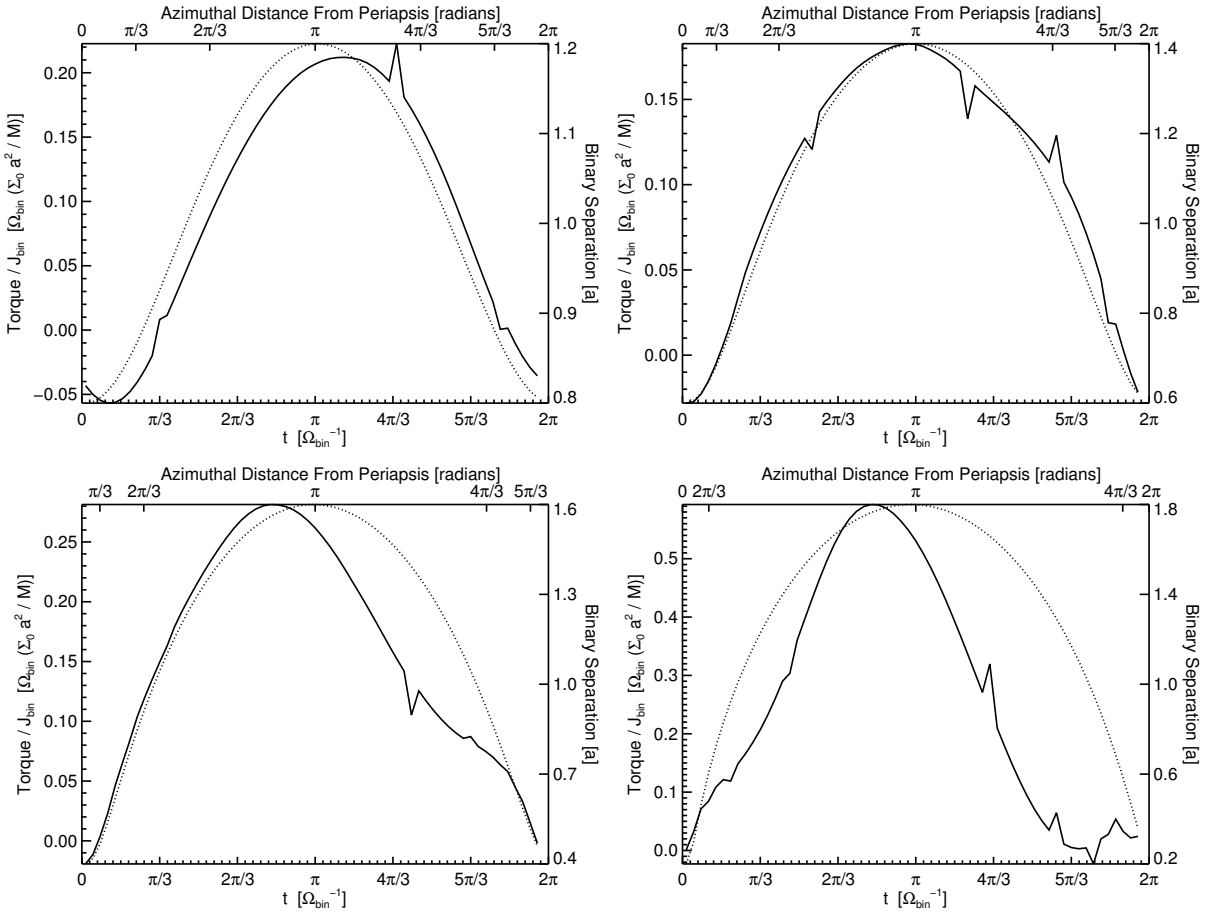

Figure 4.10: Ratio of the total binary-on-disk torque to the binary angular momentum ($\frac{T}{J_{bin}}$) as a function of simulation time during the analysis period, rebinned into a single binary orbit, with the adjusted data points being the average of the raw data in each bin. The jagged sections are caused by bins with too few data points to create a smooth average. Top Left: e = 0.2, Top Right: e = 0.4, Bottom Left: e = 0.6, Bottom Right: e = 0.8. The dotted curve shows the binary separation as the binary moves from periapsis to apoapsis and back. The axis on top of the plots displays the binary's angular position relative to periapsis. Note that the scales for $\frac{T}{J_{bin}}$ and binary separation change for each graph.

Continuing our discussion on accretion streams, we now look in detail at how binary torques repel the streams. During the binary descent phase, the azimuthal velocity of the accretion streams remains relatively constant. The azimuthal velocity of the binary, however, grows as the binary separation decreases. Eventually, the binary achieves a greater azimuthal velocity than the gas in the accretion streams. Once this occurs, the streams will gradually pass from the negative torque quadrants ahead of the binary to the positive torque quadrants behind the binary. Small eccentricity binaries have relatively large separations when this transition occurs. The larger binary separation means a shorter distance between the binary and the streams, and thus a greater positive torque magnitude. These positive torques are powerful enough to propel the portion of the gas streams which have not passed beyond the boundary outward into the gap region. Conversely, large eccentricity binaries are at relatively small separations during this transition which means that the positive torques are weaker than in the case of small eccentricity binaries. These weaker torques are less efficient at propelling the unaccreted portion of the gas streams back into the gap region. The accretion streams are eventually repelled during the ascent phase of the binary's next orbit.

Accretion streams form in a similar, but reversed manner. During the binary ascent phase, as the binary approaches apoapsis, its azimuthal velocity decreases (in the case of large eccentricity binaries, significantly so). As this happens, fluid is able to pass from the positive torque quadrant behind the binary members into the negative torque quadrant ahead of them. The negative torque strips angular momentum from the streams causing them to move inward toward the binary region.

4.3.2 Specific Angular Momentum of Accreted Gas

We define the specific angular momentum of the matter passing through the inner boundary to be:

$$j_{in} \equiv \frac{\int \Sigma\, v_r\, v_\phi\, r^2\, d\phi}{\int \Sigma\, v_r\, r\, d\phi} \tag{4.3}$$

The specific angular momentum of the matter accreted through the inner simulation boundary, time averaged over the analysis period, is (1.01, 1.08, 1.21, 1.34) $[\Omega_{bin}\, a^2]$. for eccentricities (0.2, 0.4, 0.6, 0.8) respectively. It is illustrative to compare these average specific angular momentum values with the specific angular momentum of the binary. The ratio of specific angular momentums $\frac{j_{in}}{j_{binary}}$ is (4.5, 5.6, 7.7, 12) for eccentricities (0.2, 0.4, 0.6, 0.8) respectively. These ratios show a monotonic increase with increasing binary eccentricity. The implication is that, in general, material crossing from a circumbinary disk into the region of a binary with a larger orbital eccentricity will carry more angular momentum per unit mass as compared to the specific angular momentum of the binary itself.

In Figure 4.11 we present the ratio of the specific angular momentum of matter crossing the inner boundary material to that of the central binary. Peaks occur when binary-on-disk torques impart angular momentum to the streams as they pass through positive torque quadrants. The falloffs in the graph occur when angular momentum in the streams is either extracted by binary-on-disk torques as the streams move through negative torque quadrants or is lost through shocks during collions with inner regions of the main disk (as described in SK12). The specific angular momentum for the $e = 0.2$ and $e = 0.4$ disks peaks near periapsis because the accretion streams in

these cases have their largest amount of angular momentum after positive torques repel them during the binary descent phase. The specific angular momentum in the $e = 0.8$ disk does not have a large peak near periapsis because the positive torques during the descent phase are insufficient to repel the accretion streams. The peak instead occurs just before apoapsis because the streams get repelled during binary ascent phase. The 0.6 disk is an intermediate case between these two groups.

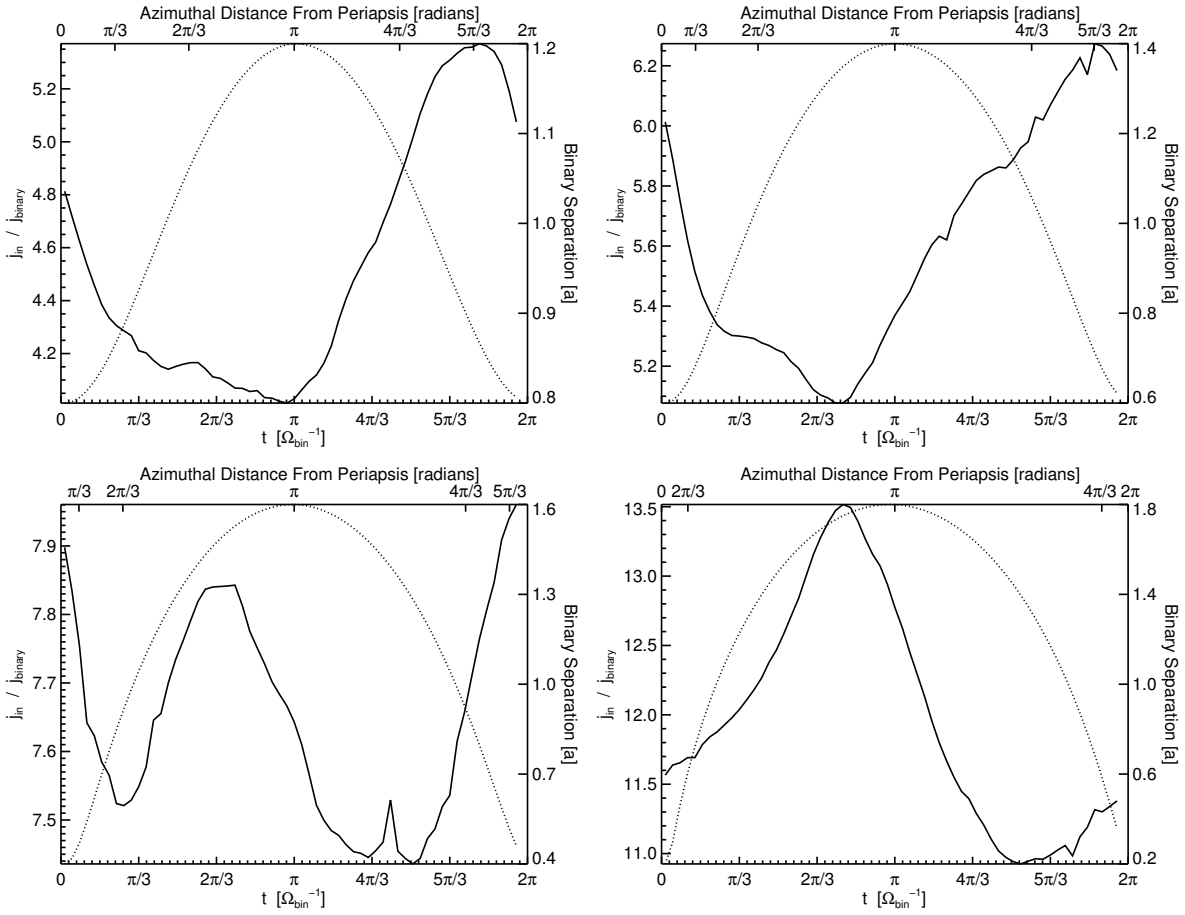

Figure 4.11: Angular momentum per unit mass at the inner computational boundary as a function of simulation time, rebinned into a single binary orbit, with the adjusted data points being the bin average of the simulation data during the analysis period. Top Left: e = 0.2, Top Right: e = 0.4, Bottom Left: e = 0.6, Bottom Right: e = 0.8. The dotted curve shows the radial separation of the binary as it moves from periapsis to apoapsis and back. The axis on top of the plots displays the binary's angular position relative to periapsis. Note that the scales change for each graph.

4.3.3 Angular Momentum Evolution

We assume that all the mass passing through the inner boundary is captured by the binary. (In the following section, we show this to be a poor assumption. However, it is neccesary to estimate binary evolution.) Thus, the time rate of change of the binary's angular momentum divided by the binary's total angular momentum yields:

$$\frac{\dot{J}}{J} = \frac{(1+q)^2 \left(\dot{M}\, j_{in} - T\right)}{q\sqrt{G\, M^3\, a\, (1-e^2)}} \tag{4.4}$$

We plot this ratio rebinned into a single binary orbit in Figure 4.12 . Averaged over the analysis period, we find a monotonic increase in the angular momentum evolution rate $\dot{J}$ (-0.0021, 0.0083, 0.025, 0.032) $[GMa\Sigma_0]$ as well as the ratio of the evolution rate to the binary angular momentum $\frac{\dot{J}}{J_{bin}}$: (-0.009, 0.037, 0.13, 0.22) $\left[\Omega_{bin}\, \frac{\Sigma_0\, a^2}{M}\right]$ with increasing eccentricity (0.2, 0.4, 0.6, 0.8) respectively. It is important to note that the average in the $e = 0.2$ case is an order of magnitude smaller than the peak values seen in Figure 4.12 and thus the negative nature of the value is not likely to be important as the magnitude is essentially negligable. These results show that the net effect of a prograde circumbinary disk is to increase (or at least not to decrease) the binary orbital angular momentum. In this, we agree with the findings of SK12, RS14 and Miranda et al. (2016). Furthermore, we find that increasing the binary orbital eccentricity enhances the rate of change of the binary's angular momentum, this was also found to be the case by Miranda et al. (2016). Finally, for all binary eccentricities, we found a minimum in the angular momentum growth during the binary's ascent phase. This minimum is due to the low rate of mass accretion which occurs during this portion of the binary orbit. Finally, we find $\frac{(\dot{j_{binary}})}{j_{binary}} = \frac{\dot{J}}{J} - \frac{\dot{M}}{M}$ to be

(-0.054, 0.13, 0.58, 1.39) $\left[\Omega_{bin}\,\frac{\Sigma_0\,a^2}{M}\right]$ for eccentricities (0.2, 0.4, 0.6, 0.8) respectively.

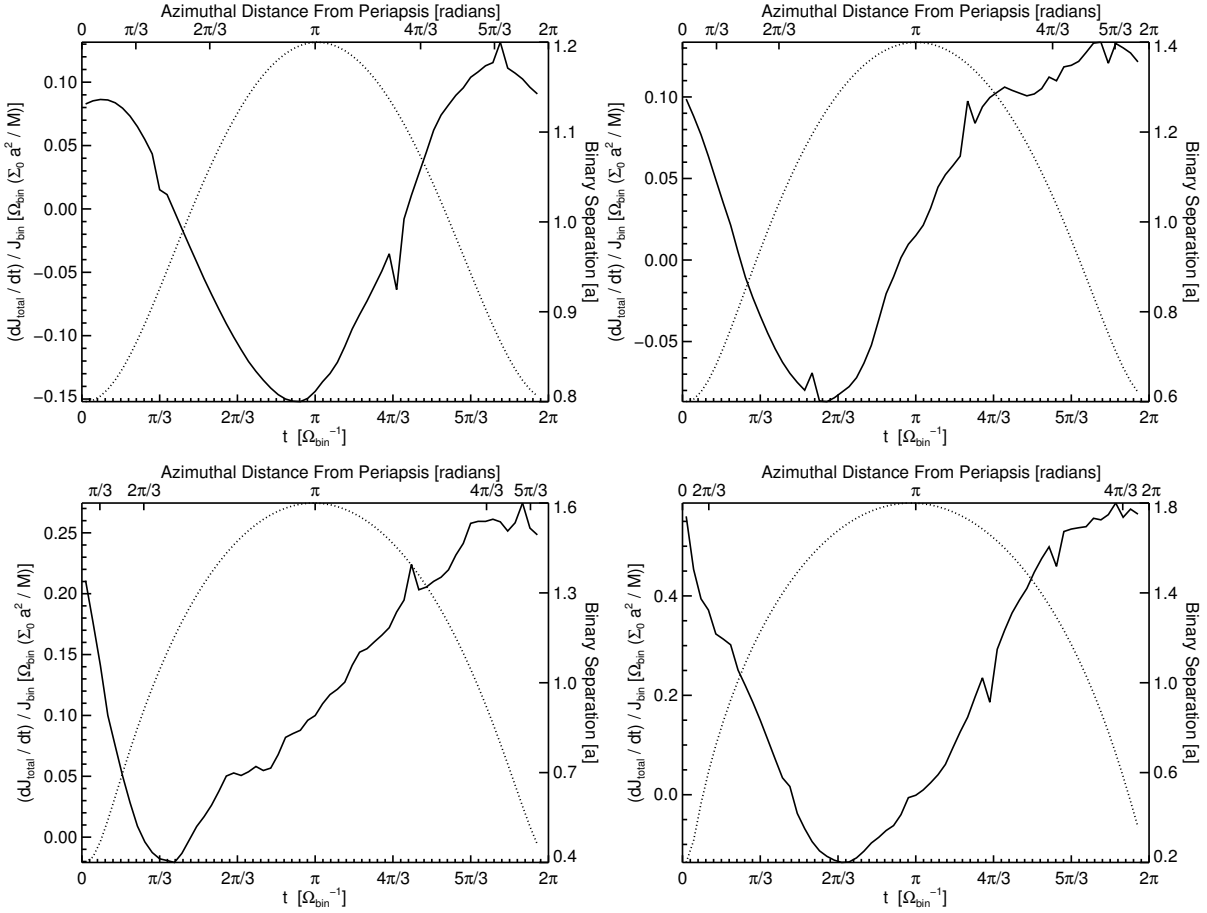

Figure 4.12: Ratio of change of the binary's total angular momentum to the binary's total angular momentum as a function of simulation time, rebinned into a single binary orbit, with the adjusted data points being the average of the raw data in each bin. Top Left: e = 0.2, Top Right: e = 0.4, Bottom Left: e = 0.6, Bottom Right: e = 0.8. The dotted curve shows the radial separation of the binary as it moves from periapsis to apoapsis and back. The axis on top of the plots displays the binary's angular position relative to periapsis. Note that the scales change for each graph.

4.4 Binary Energy Evolution

The change in the binary's orbital energy is given by the expression:

$$\frac{dE}{dt} = \frac{dE_{\dot{M}}}{dt} + \frac{dE_c}{dt} - \frac{dE_{\rm grav}}{dt} \tag{4.5}$$

which is the sum of the contributions from: (1) The change in the binary's orbital gravitational potential energy due to mass accretion, (2) the work done by the collision of the binary members with the accreting gas streams, and (3) the work done by the force of gravity on the disk material. These contributions are defined as follows:

$$(1) \quad \frac{dE_{\dot{M}}}{dt} = -\frac{G\,M^2}{s}\,\frac{q}{(1+q)^2}\left[2\,\frac{\dot{M}}{M} + \frac{1-q}{1+q}\,\dot{q}\right] \tag{4.6}$$

is the time derivative of the potential energy $E_p = -\frac{G\,M^2}{s}\,\frac{q}{(1+q)^2}$, where G is the gravitational constant, M is the binary mass, s is the binary separation, and q is the binary mass ratio. For our work $q = 1$, the $\dot{q}$ term vanishes.

$$(2) \quad \frac{dE_c}{dt} = \dot{\vec{p}}_{gas} \cdot \vec{v}_{bin} = |\vec{p}_{gas}|\;|\vec{v}_{bin}|\,\cos(\psi) \tag{4.7}$$

is the work done by accretion streams on the binary members when colliding. Here, $\vec{p}_{gas}$ is the momentum of the accretion streams, $\vec{v}_{bin}$ is the velocity of the binary members, and ψ is the impact angle. This expression assumes that all the stream mass becomes bound to the partner whose disk it strikes. The accretion stream momentum is given by $\left|\dot{\vec{p}}_{gas}\right| = \left|-\int_\phi \Sigma_{in}\,r_{in}\,v_r\,\sqrt{v_r^2+v_\phi^2}\,d\phi\right|$

$$(3) \quad \frac{dE_T}{dt} = \vec{F}_{\rm grav} \cdot \vec{v}_{\rm gas} = \left(\vec{F}_{\rm grav} \cdot \hat{r}\right) v_r + \left(\vec{F}_{\rm grav} \cdot \hat{\phi}\right) v_\phi$$

$$\vec{F}_{\rm grav} \cdot \hat{r} = \frac{G\,M\,\Sigma}{4} \frac{1}{r} \left[\frac{\frac{s^2}{4} - r_1^2 - r^2}{r_1^3} + \frac{\frac{s^2}{4} - r_2^2 - r^2}{r_2^3} \right] \tag{4.8}$$

$$\vec{F}_{\rm grav} \cdot \hat{\phi} = \frac{G\,M\,\Sigma}{4}\, s \left[\frac{\sin(\phi_1 - \phi)}{r_1^3} + \frac{\sin(\phi_2 - \phi)}{r_2^3} \right]$$

is the (per unit area) work done by the binary to the disk gas through gravitational forces. Here, v_r and v_ϕ are the radial and azimuthal components of the gas velocity, s is again the binary separation; Σ is the gas surface density, and r_i is the distance from the ith binary member. In the following subsections, we discuss the nature and effect of each contribution.

4.4.1 Binary-Stream Collision Contribution

We are unable to track matter after it passes through the inner computational boundary, thus to estimate what a reasonable impact angle may be, we performed simple ballistic calculations with the binary members on fixed elliptical orbits and a test particle able to move freely under the gravitational influence of the binary. The use of a test particle to represent stream material near the binary is justified because gravitational forces will dominate gas motion in this regime. The initial velocity and azimuthal position of the test particle were given to be the density weighted averages of those quantities, from the 3D MHD simulations, for a population of the matter passing through the inner boundary which met certain cuts in $\left|\frac{v_r}{v_\phi}\right|$. The binary's initial azimuthal position was set near the location where the majority of accretion occurs for the given eccentricity ($\frac{7\,\pi}{6}$ for $e = 0.2$ and π for the other eccentricities). A

target around each binary member of size $0.3\,a\,(1-e)$ was used to emulate the mini-disks which would likely be present (The size of the target is based on our discussion of mini-disks in 3.4 modified to account for the smaller separation at periapsis).

The calculations used kinematic equations:

$$\begin{aligned} \vec{a}_p &= -\frac{G\,M}{2}\left[\frac{\hat{r}_1}{|\vec{r}_1|^2}+\frac{\hat{r}_2}{|\vec{r}_2|^2}\right] \\ \vec{v}_p &= \vec{v}_{p,0}+\vec{a}_p\,\Delta t \\ \vec{s}_p &= \vec{s}_{p,0}+\vec{v}_p\,\Delta t+\frac{1}{2}\,\vec{a}_p\,(\Delta t)^2 \end{aligned} \tag{4.9}$$

to update the test particle's position and velocity based on the binary's gravitational force with a time step of $\Delta t = \frac{10^{-5}}{\Omega_{bin}}$. For the $e = 0.2$ case, a Δt of $\frac{10^{-6}}{\Omega_{bin}}$ was used to refine the results. Here, $\vec{r}_1$ is the relative position vector between the particle and mass 1, $\vec{r}_2$ is the relative position vector between the particle and mass 2, $\vec{a}_p$ is the particle's acceleration, $\vec{v}_p$ is the particle's velocity, and $\vec{s}_p$ is the particle's position. The (0) subscript indicates that the value from the previous iteration is used. G and M (the total binary mass) were set to be unity and distances had units of a. This was done so that the calculation units were the same as the 3D MHD simulation units. The calculations were run for the length of a single binary orbit.

In the ballistic runs, we found some material accreted onto the nearer binary member, while the rest either accreted onto the far binary member, or did not accrete at all in the time span of the calculations. It is legitimate to follow the test-particle orbit to the nearer binary member, possible but speculative to follow it to the farther binary member, but probably not a good idea to follow it any farther. This is because the longer that gas remains in the central binary region, the greater the chance that collisions will occur with other gas occupying the region. These collisions would

mix angular momentum and dissipate energy in ways that our ballistic calculations cannot account for. For this reason, we consider mass that attaches to the near binary member in our binary evolution model.

Table 4.1 shows the results of the ballistic calculation. The table records the cosine of the impact angle between the test particle's velocity and the accreting binary member's velocity as well as the mass percentage that each population cut represents. From this data, we conclude that for $e > 0.3$, the majority of the material misses the nearest binary member's mini-disk. Thus, while we can speak with some confidence about the stream collision contribution to the energy evolution of a $e = 0.2$ binary, our results for the orbital energy evolution of more eccentric binaries will be less definitive.

Beyond insights into the impact angles for the $e = 0.2$ disk, one interesting result of the data is the relationship between binary eccentricity and the velocity distribution of matter at the inner edge of the computational zone. $\left|\frac{v_r}{v_\phi}\right|$ has a larger spread for lower binary eccentricity and tightens up at smaller values as eccentricity increases. A possible reason for this, is that larger eccentricity binaries are not able to repel accretion streams as well as smaller eccentricity binaries can and the stream material continues to orbit in the gap region without as much radial motion as in the case of smaller eccentricity binaries. We discuss this in more detail in the previous section.

Figure 4.13 shows the contribution to the energy evolution due to the gas streams impacting the binary as it varies with the cosine of the impact angle. Our ballistic calculations give us an idea of likely impact angles for $e = 0.2$ binaries based off of the average characteristics of populations of matter passing through the inner computational boundary. For this reason, we limit our examination of the $e = 0.2$ case to small impact angles. For the other eccentricities, The impact angle is allowed

to vary from 0 (parallel; least amount of orbital energy dissipated into heat) to (anti-parallel; most amount of orbital energy dissipated into heat). For this plot, we assume that matter attaches to the mini-disk of the near binary member and that neither $\dot{\vec{p}}$ nor $\vec{v}_{bin}$ changes appreciably between the moment of boundary crossing and the moment at which the stream reaches that mini-disk. These assumptions are not good for $e > 0.3$, but they are neccesary for us to continue our analysis. Allowing the first assumption, the second is actually fairly acceptable. From the ballistic calculations of the $e = 0.2$ case, where most of the material did attach to the nearest binary member, the ratio of $\frac{|\vec{p}_{accrete}|}{|\vec{p}_{initial}|} \simeq 1.1$ for populations $\left|\frac{v_r}{v_\phi}\right| \geq 0.6$, representing $\sim 66\%$ of the successfully accreted mass. The ratio rose to $\simeq 2 - 3$ for bins at the low end of the $\left|\frac{v_r}{v_\phi}\right|$ range. Because of these assumptions, the model is more appropriate near apoapsis. These plots show that, for smaller eccentricities, the bulk of the stream collision contribution to the energy evolution occurs in the binary descent phase. For larger eccentricity binaries, the time near apoapsis does not yield much contribution to the change in binary orbital energy. The time averaged values of this energy contribution are (0.078 $\pm$ 0.02, 0.095 $\pm$ 0.03, 0.13 $\pm$ 0.03, 0.14 $\pm$ 0.05) $\left[\Omega_{bin}\,\frac{\Sigma_0\,a^2}{M}\right]$ for eccentricities (0.2, 0.4, 0.6, 0.8) respectively. The uncertainty arises purely from the uncertainty in $\cos(\psi)$.

	e = 0.2		**e = 0.4**		**e = 0.6**		**e = 0.8**	
$\left\lvert\frac{v_r}{v_\phi}\right\rvert$	$\cos\psi$	Mass %	$\cos\psi$	Mass %	$\cos\psi$	Mass %	$\cos\psi$	Mass %
0.00 - 0.05	0.96	2.1	0.91	3.1	0.85	1.2	-0.35*	2.7
0.05 - 0.10	0.97	3.6	-	4.8	-	5.4	-	9.2
0.10 - 0.15	0.92	3.5	-	5.4	0.71	6.0	-	9.3
0.15 - 0.20	-	4.0	0.54	5.6	0.46*	6.2	-	9.8
0.20 - 0.25	0.17	4.9	-0.16*	5.9	-	6.7	-	10.4
0.25 - 0.30	-.08*	5.1	-	5.8	-	7.7	-	12.3
0.30 - 0.35	-	4.4	-	5.9	-	9.4	-	12.8
0.35 - 0.40	-	4.9	-	5.8	-	10.5	-	10.9
0.40 - 0.45	-	5.6	-	7.1	-	11.7	-	9.0
0.45 - 0.50	-	6.1	-	8.1	-	11.8	0.054*	6.0
0.50 - 0.55	-	6.8	-	8.3	-	8.7	-0.27*	3.5
0.55 - 0.60	-	7.0	-	7.5	-	5.5	-0.70*	2.0
0.60 - 0.65	1.0	7.3	-	6.4	0.68	3.7	-	1.1
0.65 - 0.70	0.96	7.8	-	5.3	-	2.6	-	0.5
0.70 - 0.75	0.90	6.7	-	4.2	0.98	1.4	0.71*	0.3
0.75 - 0.80	0.93	5.2	-	3.5	0.96*	0.7	1.0	0.1
0.80 - 0.85	0.93	4.1	0.72	2.8	0.87	0.4	-	0.0
0.85 - 0.90	0.81	3.1	0.18	1.6	0.99	0.2	-	0.0
0.90 - 0.95	0.78	2.4	0.79	1.1	0.93	0.1	-	0.0
0.95 - 1.00	0.78	2.0	0.78	0.8	-	0.0	-	0.0
1.00 - 1.05	0.91	1.5	0.80	0.5	-	0.0	-	0.0
1.05 - 1.10	0.81	1.0	0.88	0.3	-	0.0	-	0.0
% Accreted		60.3		21.7		19.9		14.6

Table 4.1: The results of accretion of the test particle onto binary members during the ballistic calculations. The left most column denotes the cut conditions for the population contributing to the test particle's initial conditions. The other columns are grouped in pairs for each binary eccentricity investigated. The left pair member gives the cosine of the impact angle (ψ) and the right pair member gives the percentage of the accreted mass that the contributing population represents. Asterisks indicate that accretion occured onto the far binary member. Dashes indicate that the test particle did not accrete. The bottom of the table lists, for each eccentricity, the percentage of the mass that passed into the binary region which is successfully accreted in a single binary orbit.

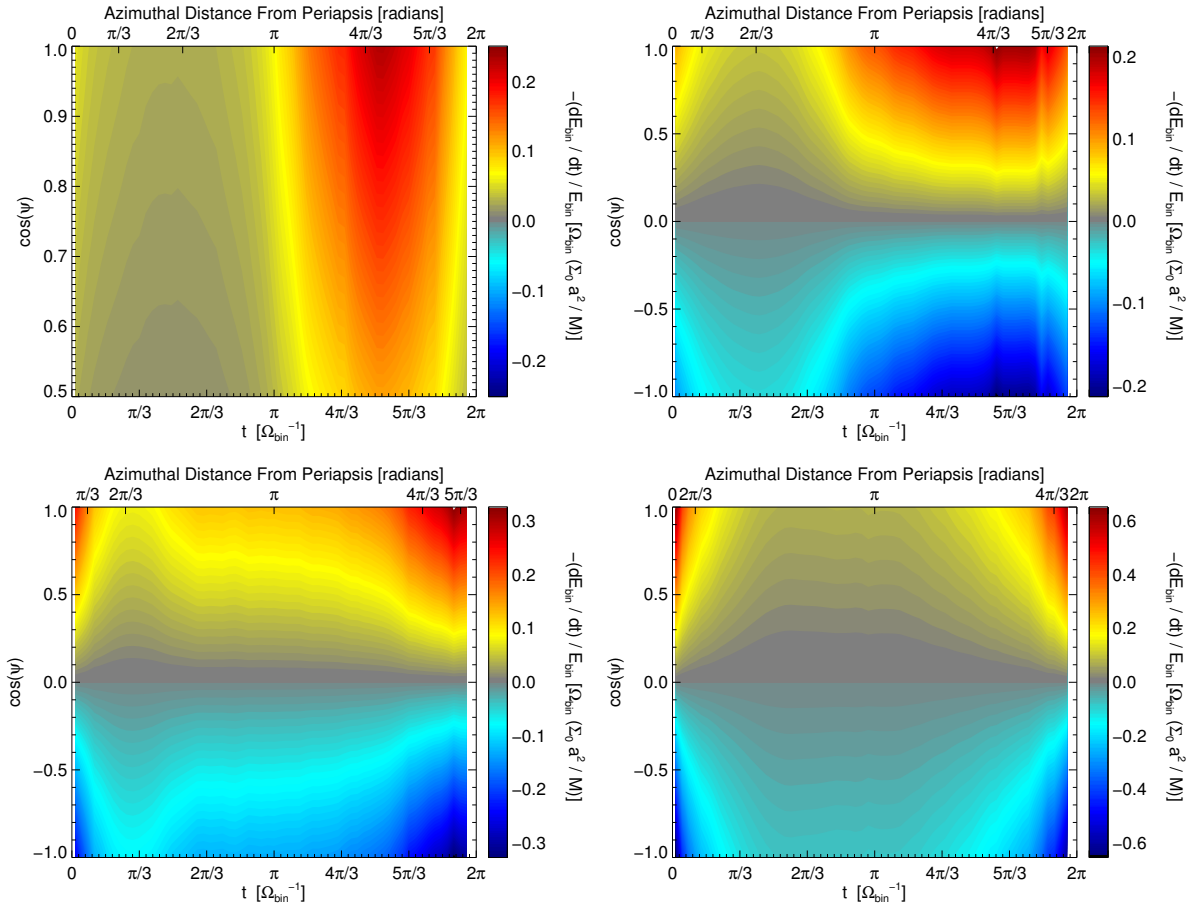

Figure 4.13: $-\frac{\dot{E}_{bin}}{E_{bin}}$ contribution from stream-binary collisions as a function of simulation time, rebinned into a single binary orbit, with the adjusted data points being the bin average of the simulation data during the analysis period. The y-axis of these plots denotes the cosine of the impact angle between the momentum of the accreted gas and the velocity of the binary. Top Left: e = 0.2, Top Right: e = 0.4, Bottom Left: e = 0.6, Bottom Right: e = 0.8. Note that the scales change for each graph. The axis on top of the plots displays the binary's angular position relative to periapsis. The vertical stripes are the result of underfilled bins.

4.4.2 Mass Accretion Contribution

Figure 4.14 shows the change in potential energy due to mass accretion, which arises directly from the mass accretion rate (See Equation 4.6). Our assumption (dubious for $e > 0.3$) is that the material accretes onto the nearest binary member while it is near apoapsis. The time averaged values of this energy contribution are (-0.074, -0.11, -0.17, -0.23) $\left[\Omega_{bin}\,\frac{\Sigma_0\,a^2}{M}\right]$ for eccentricities (0.2, 0.4, 0.6, 0.8) respectively.

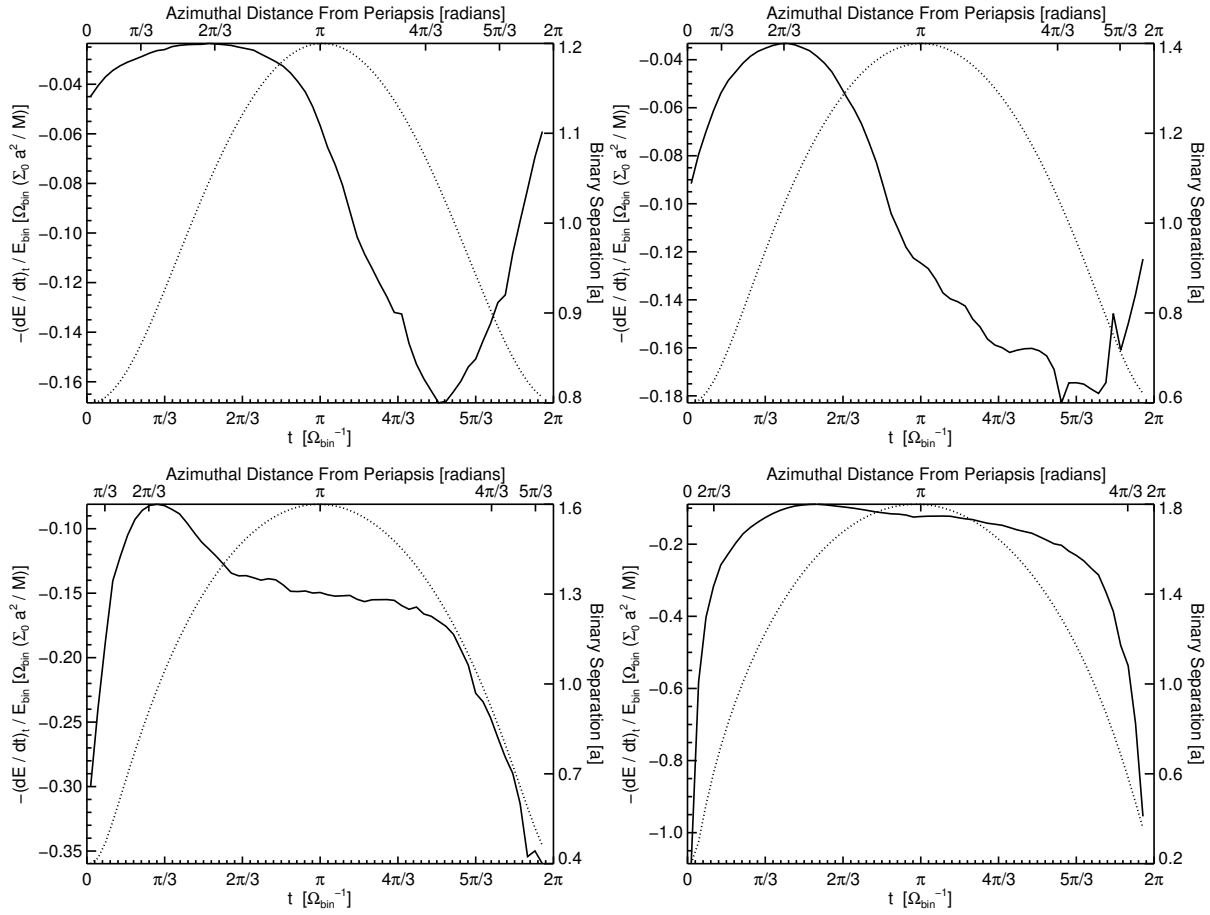

Figure 4.14: $-\frac{\dot{E}_{bin}}{E_{bin}}$ contribution from mass accretion as a function of simulation time, rebinned into a single binary orbit, with the adjusted data points being the average of the raw data in each bin. The jagged sections are caused by bins with too few data points to create a smooth average. Top Left: e = 0.2, Top Right: e = 0.4, Bottom Left: e = 0.6, Bottom Right: e = 0.8. The dotted curve shows the radial separation of the binary as it moves from periapsis to apoapsis and back. The axis on top of the plots displays the binary's angular position relative to periapsis. Note that the scales for $-\frac{dE}{dt}$ and binary separation change for each graph.

4.4.3 Gravitational Work Contribution

Figure 4.15 shows the ϕ-component of the gravitational work per area on the disk. The work magnitude diminishes as eccentricity increases. The bulk of this work is done on mid-regions of the accretion streams in positive torque quadrants. Some (difficult to calculate how much) of the uncertainty from neglecting work done in the cut-out is cancelled by using the boundary crossing value of $\dot{p}_{gas}$ for the collisions. presumably the streams gain kinetic energy when they move closer to the binary.

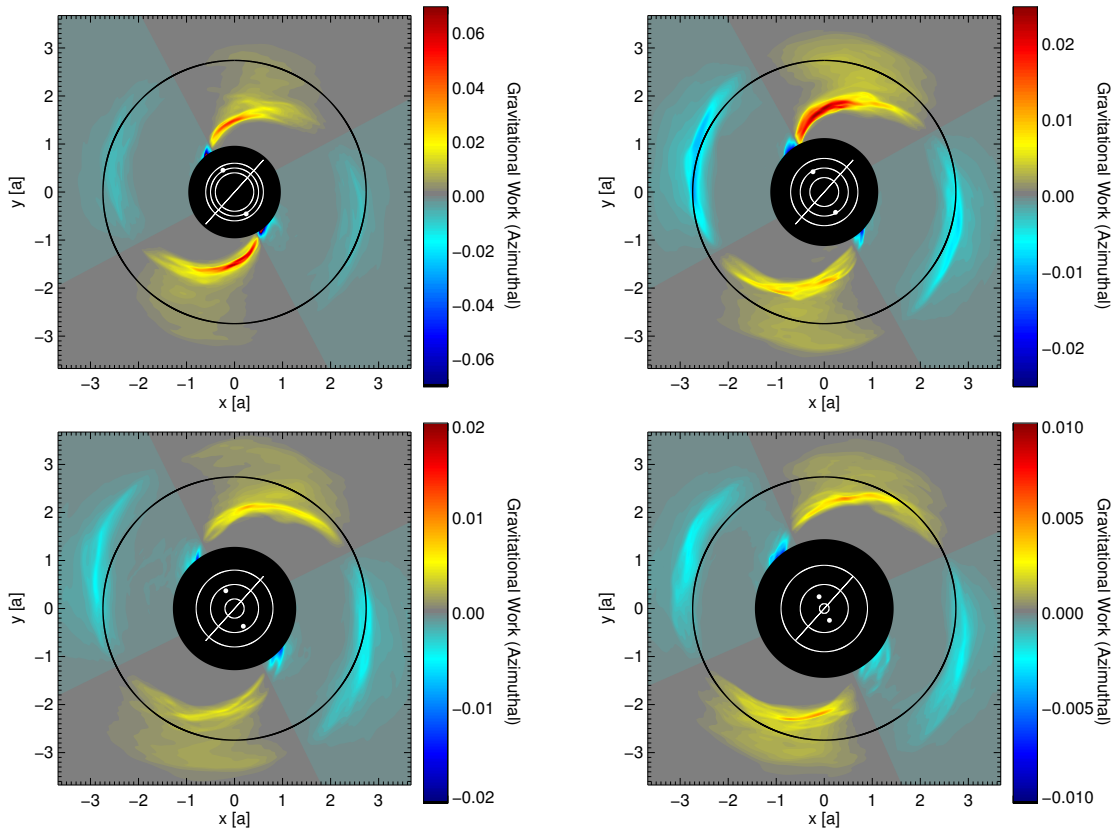

Figure 4.15: Azimuthal component of the gravitational work done on the disk by the binary. Top Left: e = 0.2, Top Right: e = 0.4, Bottom Left: e = 0.6, Bottom Right: e = 0.8. The inner white ring denotes the minimum binary orbital radius. The middle white ring has a diameter equal to the semi-major axis of the binary orbit. The outer white ring denotes the maximum binary orbital radius. The solid black ring denotes the position of the shell and time averaged maximum of the disk surface density. The solid white line indicates the orientation of the binary at periapsis and apoapsis. In the images and the color scale, blue tones indicate negative work on the disk while yellow and red tones indicate positive.

Figure 4.16 shows the change in binary energy from the azimuthal component of the binary-on-disk gravitational work. The bulk of the work is done in the positive torque regions, which results in a loss of energy for the binary. The magnitude of this contribution peaks when the binary is near apoapsis and the accretion streams are crossing the gap region. The time averaged values of this energy contribution are (-0.094, -0.079, -0.10, -0.15) $\left[\Omega_{bin}\,\frac{\Sigma_0\,a^2}{M}\right]$ for eccentricities (0.2, 0.4, 0.6, 0.8) respectively.

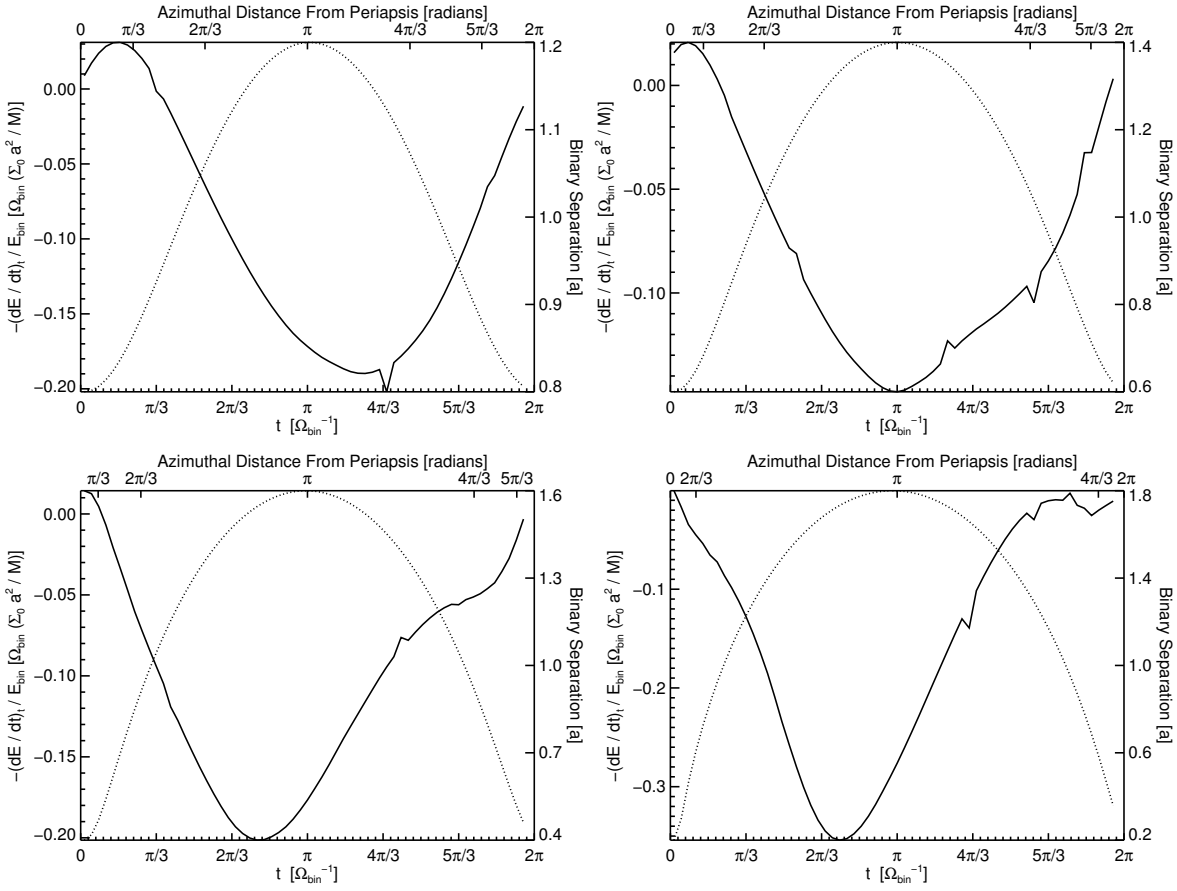

Figure 4.16: $-\frac{\dot{E}_{bin}}{E_{bin}}$ contribution from the azimuthal component of the binary-on-disk gravitational work as a function of simulation time, rebinned into a single binary orbit, with the adjusted data points being the average of the raw data in each bin. The jagged sections are caused by bins with too few data points to create a smooth average. Top Left: e = 0.2, Top Right: e = 0.4, Bottom Left: e = 0.6, Bottom Right: e = 0.8. The dotted curve shows the radial separation of the binary as it moves from periapsis to apoapsis and back. The axis on top of the plots displays the binary's angular position relative to periapsis. Note that the scales for $-\frac{dE}{dt}$ and binary separation change for each graph.

Figure 4.17 shows the (per unit area) work done on the disk by the radial component of the binary gravitational force. The blue regions in these plots show the inward flow of material along the accretion streams. The red and yellow regions show material expelled from previous accretion streams moving outward. These processes help to form the spiral density waves seen in the disk midplane.

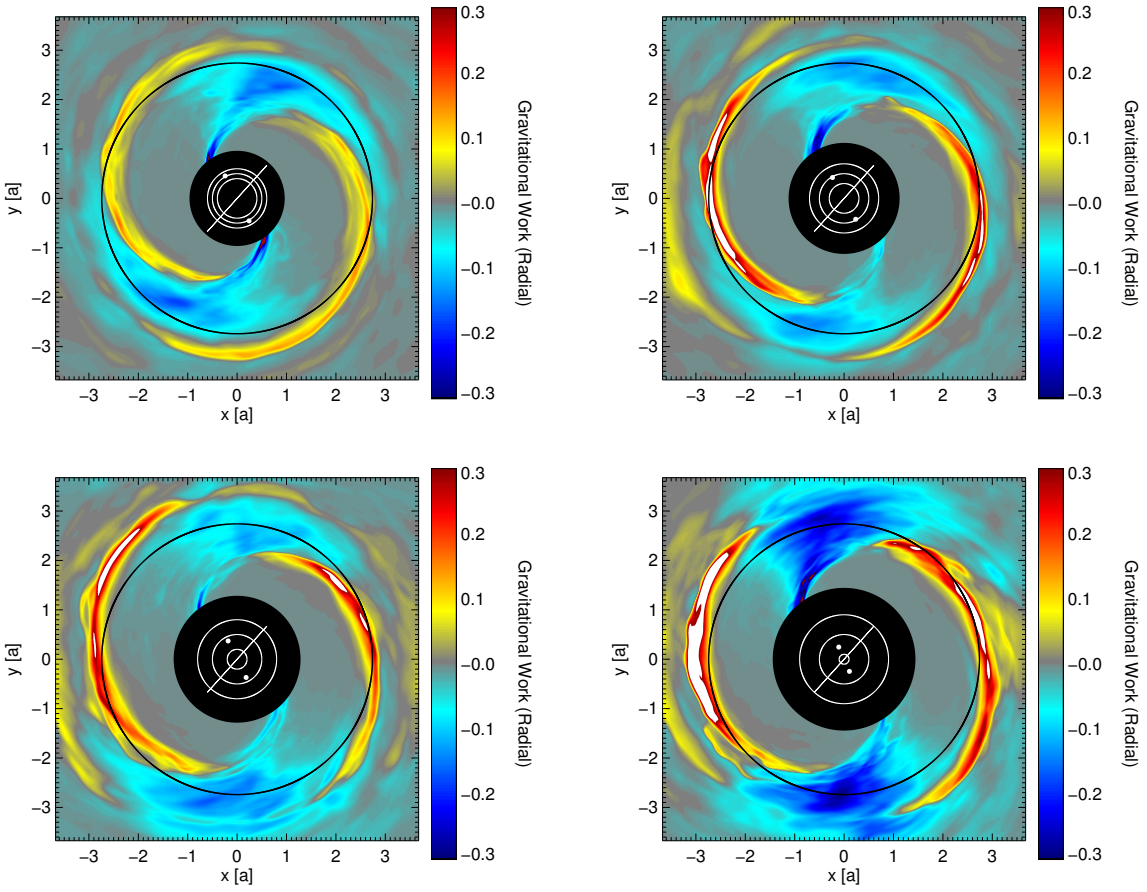

Figure 4.17: Radial component of the gravitational work done on the disk by the binary. Top Left: e = 0.2, Top Right: e = 0.4, Bottom Left: e = 0.6, Bottom Right: e = 0.8. The inner white ring denotes the minimum binary orbital radius. The middle white ring has a diameter equal to the semi-major axis of the binary orbit. The outer white ring denotes the maximum binary orbital radius. The solid black ring denotes the position of the shell and time averaged maximum of the disk surface density. The solid white line indicates the orientation of the binary at periapsis and apoapsis. In the images and the color scale, blue tones indicate negative work on the disk while yellow and red tones indicate positive.

Figure 4.18 shows the change in binary energy from the radial component of the binary-on-disk gravitational work. The sinusoidal pattern seen in the graphs is caused by the radial movement of accretion stream material over the course of a binary orbit. As the binary approaches apoapsis, material is pulled inward towards the binary. After a fraction of a binary orbit, binary-on-disk torques push the material radially outward again. The time averaged values of this energy contribution are (-0.24, -0.26, -0.33, -0.42) $\left[\Omega_{bin}\,\frac{\Sigma_0\,a^2}{M}\right]$ for eccentricities (0.2, 0.4, 0.6, 0.8) respectively.

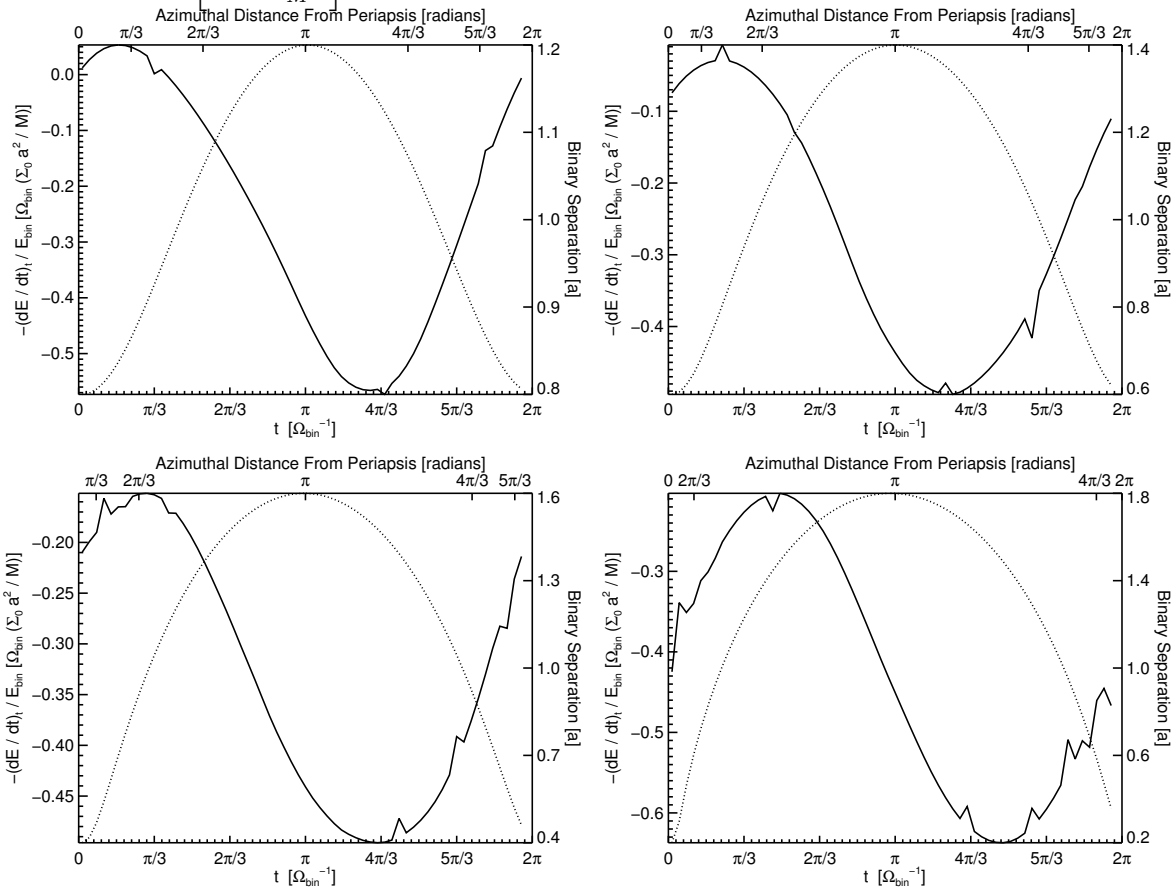

Figure 4.18: $-\frac{\dot{E}_{bin}}{E_{bin}}$ contribution from the radial component of the binary-on-disk gravitational work as a function of simulation time, rebinned into a single binary orbit, with the adjusted data points being the average of the raw data in each bin. The jagged sections are caused by bins with too few data points to create a smooth average. Top Left: e = 0.2, Top Right: e = 0.4, Bottom Left: e = 0.6, Bottom Right: e = 0.8. The dotted curve shows the radial separation of the binary as it moves from periapsis to apoapsis and back. The axis on top of the plots displays the binary's angular position relative to periapsis. Note that the scales for $-\frac{dE}{dt}$ and binary separation change for each graph.

4.4.4 Energy Evolution

We now consider the sum of the contributions for the binary orbital energy evolution. As stated before, our ballistic calculations give us an idea of likely impact angles for $e = 0.2$ binaries based off of the average characteristics of populations of matter passing through the inner computational boundary. It is worth pointing out that, in the $e = 0.2$ case, we were only able to account for about 60% of the mass and less so for larger eccentricities. We present Figure 4.19 to show a spectrum of possible energy evolution trajectories. The plots show the change in the binary orbital energy as a function of possible impact angles over the course of a binary orbit. The time averaged total energy evolution values $(-\frac{\dot{E}}{E})$ are (-0.33, -0.35, -0.47, -0.66) $\left[\Omega_{bin}\,\frac{\Sigma_0\,a^2}{M}\right]$ for eccentricities (0.2, 0.4, 0.6, 0.8) respectively.

In Figure 4.19 , the $e = 0.2$ plot is zoomed in to show only smaller impact angles in keeping with our findings from the ballistic calculations. The right-left modulation of the plots is dominated by the contributions from the binary-on-disk gravitational work. For small eccentricities ($e < 0.5$), there is not much change in the energy evolution rate as a function of the stream-binary impact angle; the stream-binary collision contribution is sub-dominant for these binaries. For larger eccentricities, there is more balance between the different contributions resulting in a more noticeable top-bottom modulation. Note that the color scheme in these plots are all of the same scale, and almost all values are negative, indicating a decrease in binary orbital energy.

Our analysis of the binary orbital energy evolution is incomplete in several respects. First, as mentioned before, we cannot account for the majority of matter which passes through the cut-out for $e > 0.3$. We assume that this matter is captured by the binary mini-disks, but it maybe that dynamics within the cut-out propel

some of this gas into the gap region. Second, we assume that accretion occurs onto the closer binary member near apoapsis and that $\dot{\vec{p}}_{gas}$ and $\vec{v}_{bin}$ do not change between the time gas exits the simulation and accretion occurs. We cannot verify this assumption, and indeed there is evidence from our ballistic calculations that this is untrue for eccentricities larger than 0.2. Finally, we cannot calculate the work done by gravity between the time the gas crosses the cut-out and the time it attaches to a mini-disk. These caveats must be kept in mind when considering our binary orbital evolution results.

If, as we assume for our analysis, that accretion takes place at apoapsis and the values of $\dot{\vec{p}}_{gas}$ and $\vec{v}_{bin}$ are unchanged between crossing the inner computational boundary and accretion onto the binary, then the potential error from the stream collision contribution is $\sim 20\%$ of the base value for each binary eccentricity. However, as our ballistic calculations show, these are not good assumptions. We do not know the actual binary separation at the time of accretion which means that the error is likely much larger. The mass accretion contribution is also dependent on the binary separation at the time of accretion. This introduces a potential error of $\frac{1+e}{1-e}$ which grows from a factor of 1.5 for $e = 0.2$ to a factor of 9 for $e = 0.8$. It is difficult to estimate the error from the gravitational work contribution, though it is likely to be significant as Tang et al. (2017) find the largest binary torque contributions come from $r \lesssim a$.

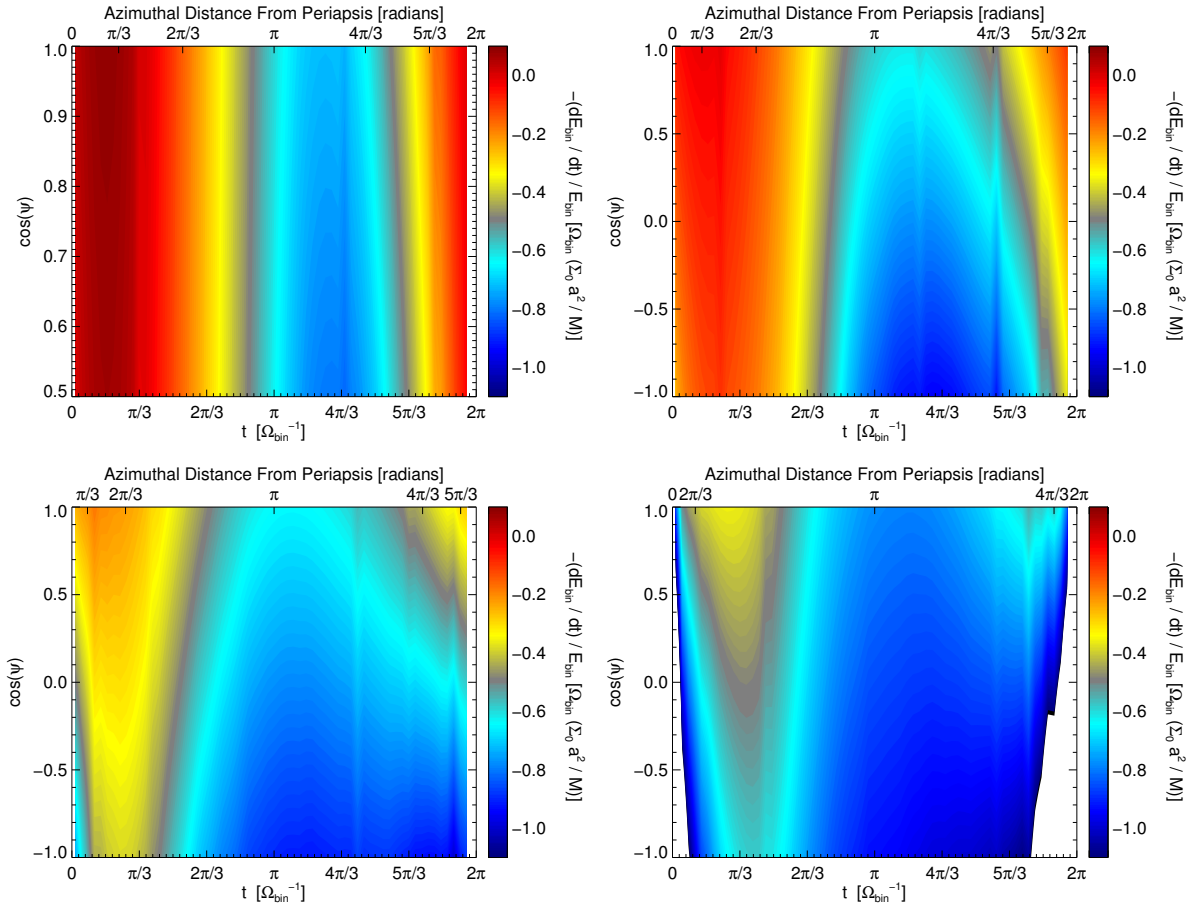

Figure 4.19: $-\frac{\dot{E}_{bin}}{E_{bin}}$ as a function of simulation time, rebinned into a single binary orbit, with the adjusted data points being the bin average of the simulation data during the analysis period. The y-axis of these plots denotes the cosine of the impact angle between the momentum of the accreted gas and the velocity of the binary. White regions denote values below the threshold of the color scale. Top Left: e = 0.2, Top Right: e = 0.4, Bottom Left: e = 0.6, Bottom Right: e = 0.8. Note that the scales change for each graph. The axis on top of the plots displays the binary's angular position relative to periapsis. The vertical stripes are the result of underfilled bins.

4.5 Orbital Eccentricity and Semi-Major Axis

Figure 4.20 shows binary orbital eccentricity evolution during a binary orbit for a range of possible impact angles. As we discussed, we are not entirely confident about our energy evolution results, especially for binary eccentricities > 0.3. Thus, for larger binary eccentricities we present a greater range of possible stream-binary impact angles. See Chapter 3.5 for more details about our binary evolution model.

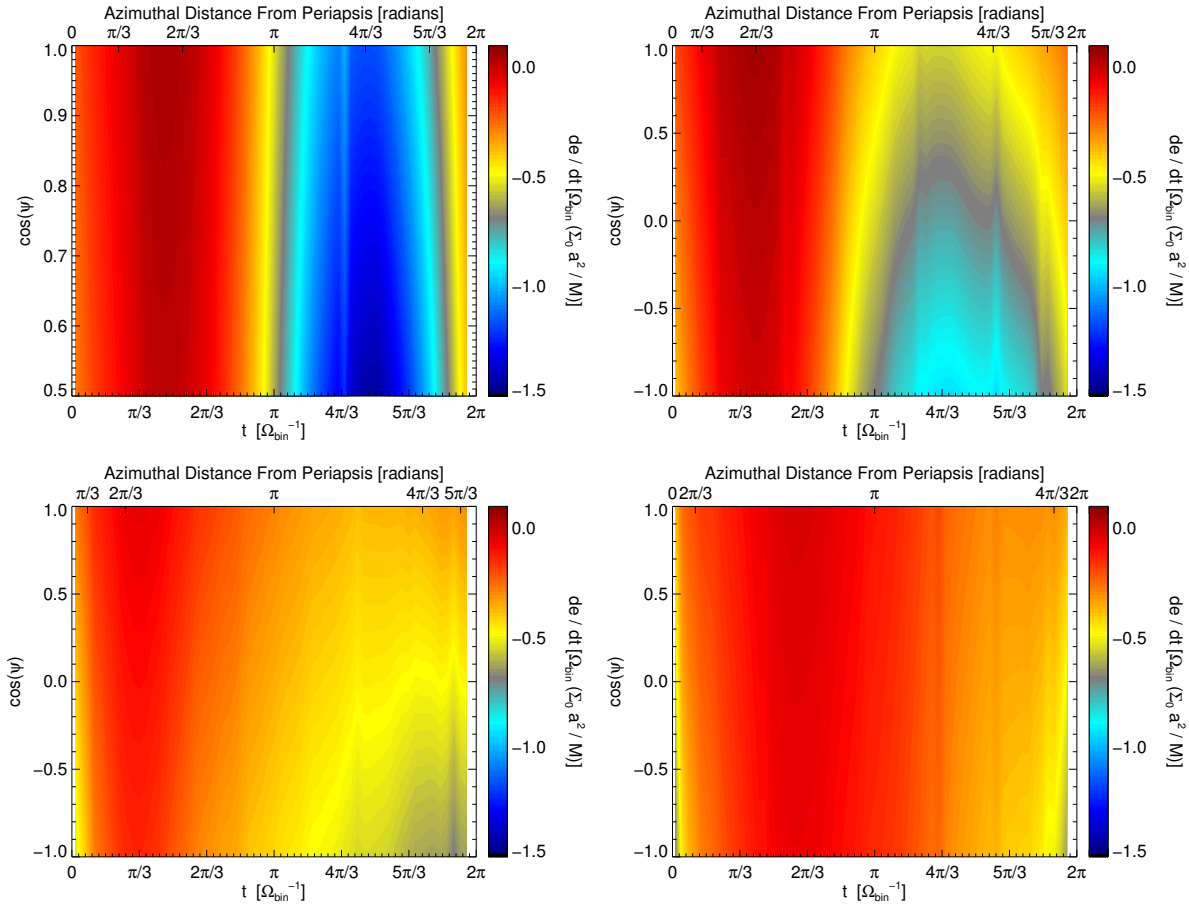

Figure 4.20: $\dot{e}$ as a function of simulation time, rebinned into a single binary orbit, with the adjusted data points being the bin average of the simulation data during the analysis period. The y-axis of these plots denotes the cosine of the impact angle between the momentum of the accreted gas and the velocity of the binary. Top Left: e = 0.2, Top Right: e = 0.4, Bottom Left: e = 0.6, Bottom Right: e = 0.8. Note that the scales for $\dot{e}$ change for each graph. The axis on top of the plots displays the binary's angular position relative to periapsis. The vertical stripes are the result of underfilled bins.

We calculate $\dot{e}$ averaged over the entire analysis period for the range of impact angles to be (-0.55 $\pm$ 0.05, -0.4 $\pm$ 0.12, -0.34 $\pm$ 0.09, -0.22 $\pm$ 0.04) $\left[\Omega_{bin} \frac{\Sigma_0 a^2}{M}\right]$ for eccentricities (0.2, 0.4, 0.6, 0.8) respectively. The uncertainty is due wholly to the factor of cos(ψ) from the collisional energy transfer. The most striking feature of these results is that all of the values are negative. This indicates that the binary energy loss rate is great enough that the binary's orbit circularizes as the semi-major axis shrinks. This also shows an inverse relation between e and the magnitude of $\dot{e}$ indicating that this circularization is more prominant for smaller binary eccentricities. Again, we caution the reader to consider the uncertainty in our energy evolution model when examining these results.

We plot the evolution of the binary orbital semi-major axis for the $e = 0.2$ binary over the course of a binary orbit and the time average for a range of impact angles in Figure 4.21 . Note, however, that our ballistic calculations suggests that the mean cos(ψ) will be not much below unity. The magnitude of $\frac{\dot{a}}{a}$ peaks during the binary descent phase because $\frac{\dot{M}}{M}$ and $-\frac{dE}{dt}$ peak during this portion of the binary orbit. The average of $\frac{\dot{a}}{a}$ over the analysis period for $e = 0.2$ is -0.3 $\pm$ 0.03 $\left[\Omega_{bin} \frac{\Sigma_0 a^2}{M}\right]$. Again, the uncertainty is due wholly to the factor of cos(ψ) from the collisional energy transfer. Due to the dependence of $\frac{\dot{a}}{a}$ on the energy evolution rate and the uncertainty in our energy evolution model, we do not attempt to infer the growth (or shrinkage) rate of the semi-major axis for eccentricities beyond $e = 0.2$.

We conclude that the inclusion of the binary region onto the computational domain is vital to future investigations into the effect of prograde circumbinary disks on eccentric binary evolution.

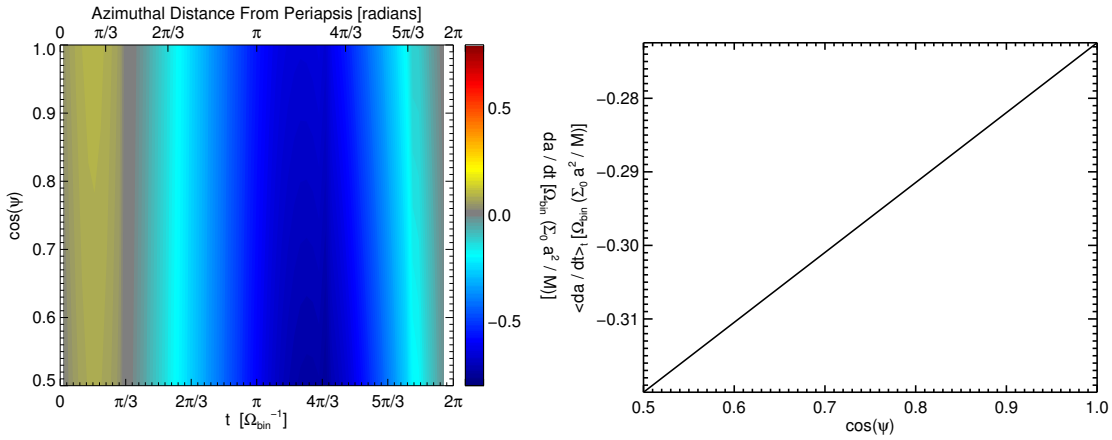

Figure 4.21: Left: $\frac{\dot{a}}{a}$ as a function of simulation time for e = 0.2, rebinned into a single binary orbit, with the adjusted data points being the bin average of the simulation data during the analysis period. The y-axis of this plot denotes the cosine of the impact angle between the momentum of the accreted gas and the velocity of the binary. The axis on top of the plot displays the binary's angular position relative to periapsis. Right: $\frac{\dot{a}}{a}$ averaged over the analysis period. The x-axis of this plot denotes the cosien of the impact angle between the momentum of the accreted gas and the velocity of the binary.

Chapter 5 Conclusions

5.1 Retrograde Circumbinary Disks

In Chapter 3 , we simulated the interactions between an equal-mass binary on a circular orbit and a surrounding circumbinary accretion disk. We are not the first to have investigated this problem: Nixon et al. (2011a) and RS14 both analyzed it with a combination of analytic arguments and simulations. Several elements of our analysis are new, however: the circumbinary disk is described in terms of 3D MHD, rather than smoothed particle hydrodynamics with either an assumed viscosity (Nixon et al., 2011a) or a disk mass large enough to be self-gravitating RS14; we analyze the internal structure of such a circumbinary disk; and we pay particular attention to the interaction between the circumbinary disk and the accretion disks that should surround the members of the binary.

In several important respects, our results agree very largely with previous work. Unlike a prograde circumbinary disk, a retrograde disk feels negligible gravitational torques from the binary, and therefore extends as close to the binary center of mass as it can before it directly touches the binary, results qualitatively similar to those of RS14. The accretion rate through its inner boundary readily comes into approximate equilibrium with the accretion rate supplied from large distance, as previously argued by Nixon et al. (2011a) and computed by RS14. Likewise, we concur with previous

authors that the addition of retrograde angular momentum to a binary whose initial eccentricity is not very large should cause rapid eccentricity growth.

However, we have also made several new points. With regard to the structure of the circumbinary disk, we have demonstrated that in the region beyond $r \sim 4a$ where the perturbative influence of the binary is small in both types of disk, the internal fluctuations, which mostly take the form of spiral waves, are very similar in character to those seen in a prograde disk. Other than the greater inward extension, the principal contrast in structure between retrograde and prograde circumbinary disks is that the dramatic break in axisymmetry seen consistently in prograde disks, often called the "lump" (Noble et al. (2012); SK12; Farris et al. (2014), does not appear at all in the retrograde case. This fact is consistent with the attribution of the lump's appearance and growth to accretion streams that pass through the gap region in prograde disks and are then flung back out (SK12). With no gap inside a retrograde circumbinary disk, this mechanism ceases to operate; in fact, the torques acting on the streams after they leave the inner edge of such a disk cause them to lose angular momentum and plunge in deeper RS14.

We have also emphasized the importance of the finite size of the accretion disks surrounding the members of the binary, particularly the secondary. This finite size guarantees continued shocks between the secondary's disk (and possibly the primary's if the mass ratio q is not too small) and the inner edge of the circumbinary disk or matter recently detached from that inner edge. In an eccentric binary, this shock heating will be periodic, raising the possibility of a signal that can be detected despite its low luminosity contrast with respect to the light generated by accretion onto the black holes. Unlike prograde circumbinary disks, the spectra of retrograde disks should not exhibit a large "notch" of the sort predicted by Roedig et al. (2014), but,

when $a(1+e) \lesssim 100R_g$, they should possess the same hard X-ray bump.

Lastly, we have clarified a few issues related to the long-term orbital evolution of such a binary. In particular, we point out that if the external mass-supply rate is the same for both retrograde and prograde cases, the accretion rate onto the binary should be roughly the same. As a result $\frac{\dot{a}}{a}$ is an order of magnitude larger for a retrograde circumbinary disk than for a prograde circumbinary disk. Furthermore, $\dot{e}$ should generically be more rapid for retrograde disks. As shown in Schnittman & Krolik (2015), this more rapid growth of eccentricity has interesting consequences for gravitational wave emission and the pace of orbital evolution.

5.2 Eccentric Binaries

In Chapter 4 , we conducted 3D, MHD simulations of prograde circumbinary accretion disks around equal mass binaries on eccentric orbits. Our work was a progression of the work performed by SK12. Wherein the first 3D, MHD simulations of prograde circumbinary accretion disks was performed. We have expanded upon that work by examining the effect of the binary orbital eccentricity on the binary orbital phase dependence of binary-disk interactions. We also speculate about the effect of the circumbinary disk on the evolution of the central binary.

Roedig et al. (2012), Goicovic et al. (2016), Rafikov (2016), and Miranda et al. (2016) have previously investigated prograde circumbinary disks around eccentric binaries using either a purely analytic approach (Rafikov, 2016), or smooth particle hydrodynamics (SPH) with either an artificial α viscocity model (Goicovic et al., 2016) or a disk mass large enough to be self-gravitating (Roedig et al., 2012), or 2D hydrodynamics (Miranda et al., 2016). However, we believe that we are the first to study in detail the binary orbital phase dependence of binary-disk interactions. The

primary strength of our work is our use of 3D MHD in simulating disk dynamics. The main weakness of our model, however, is our inability to track accreted material once it has entered the region occupied by the central binary. To gain insight into the geometry of accretion within the binary region, we performed a series of ballistic calculations which contained the binary and a test particle. The initial conditions of the test particle were given to be the density-weighted average properties of a population of material passing through the inner boundary. The populations were differentiated based on the ratio of radial inward velocity to azimuthal velocity. The results of these calculations showed that for $e > 0.3$ the majority of material crossing the inner computational boundary does not accrete onto the binary mini-disks within a single binary orbit.

Our primary finding, therefore, is that any thorough investigation into the evolution of binary systems must include a treatment of the region immediately surrounding the binary. This region is of vital importance to the evolution of the binary's orbital angular momentum and orbital energy (the two physical quantities which define the binary's orbit). Information which cannot be known by placing this region in a cutout includes 1) the manner which accretion streams impact the binary mini-disks 2) the separation of the binary when matter accretes and 3) the full effect of binary-on-gas gravitational work, which have a larger magnitude in this region than in the main body of the circumbinary disk. Despite our inability to track material past the cut-out, we successfully make phase-dependent observations of binary-disk interactions as they pertain to the material outside the binary region.

We found that, just as was discovered in SK12 the binary is fed by transient accretion streams, which peel off of the bulk disk to deposit material into the central binary region. After a time (shorter than a binary orbital period), these streams are

expelled by binary torques back into the gap region. In the case of SK12 these streams created a large non-axisymmetric build up of disk material at the inner edge of the bulk disk. This did not occur in our simulations of binary's with eccentric orbits. The accretion streams were, however, connected to $m = 2$ spiral density waves which were present in the main disk. We also found the gap region to grow in size with binary orbital eccentricity; it asymptotically approached a value of $3.2a$.

In our simulations, we found a steady, monotonic increase in the time averaged mass accretion rate through the inner boundary of the computational zone with increasing binary orbital eccentricity. We also found that, for all binary eccentricities, most mass accretion from the circumbinary disk to the binary region occurs when the binary is near apoapsis.

As was found in Tang et al. (2017) in their investigation of circular prograde circumbinary accretion disks, we observed the disk plane divided into quadrants of alternating positive and negative torque. We also observed that, as the binary neared apoapsis, extraction of angular momentum from the accretion streams as they passed through the negative torque quadrants, allowed the streams to bridge the gap region and portions of the streams to accrete into the binary region during the binary descent phase; the accretion streams traversing the gap region dominated the binary-disk torque interactions. The reason that that the streams form when the binary is near binary apoapsis as opposed to periapsis is that the decreased distance between binary and disk material near apoapsis enhances the torque magnitude. The binary azimuthal velocity increases after it passes apoapsis, eventually overtaking the accretion streams in azimuthal position. As the accretion streams pass from the negative torque quadrants ahead of the binary members to positive torque quadrants behind, the streams are expelled back into the gap region; this causes the accretion rate to

drop. The repelling of accretion streams is more pronounced for small eccentricity binaries because the binary separation is still large ($\geq a$) as the streams pass into the positive torque regions. The result of this is that smaller eccentricity binaries will have larger populations of disk material with a higher ratio of $\left|\frac{v_r}{v_\phi}\right|$, which we also observed to be true.

In agreement with SK12, RS14 and Miranda et al. (2016), we find that prograde circumbinary accretion disks have the net effect of increasing the overall angular momentum of the central binary. Furthermore, we find that the rate of binary angular momentum increase grows with binary orbital eccentricity; in agreement with Miranda et al. (2016). We also found that the binary angular momentum growth rate has a minimum during the binary ascent phase due to the lower rate of mass accretion during this part of the binary orbit. Note that we did find a negative time averaged angular momentum evolution rate for the $e = 0.2$ case. However, the magnitude of the time averaged value was two orders of magnitude smaller than the phase-dependent fluctuations. Thus the average is very close to zero.

From our ballistic calculations, we find that most of the material which accretes into the binary region is not captured by the binary mini-disks within one binary orbit for binary eccentrcities greater than ~ 0.3. Thus, while we speak with confidence about our analysis of the disk material outside the binary region, our analysis of the binary evolution is less definitive, especially for eccentricities beyond the $e = 0.2$ case.

Though our binary evolution model is neccesarily speculative, we find (in agreement with RS14) the binary semi-major axis shrinks for the $e = 0.2$ case. We do not investigate the semi-major axis evolution for eccentricities larger than $e = 0.2$ due to its heavy reliance on the energy evolution rate, which we are even less confident that our model accurately captures for larger eccentricities. In contrast to RS14, however,

we find that the effect of a prograde circumbinary accretion disk is to circularize the binary. This is possibly due to our inability to account for the evolution drivers which exist in the cutout region, however, RS14 had essentially no mini-disks for the binary to interact with and thus may have missed evolution contributions as well. Further work in this area is required in order to further refine these results.

In our simulations, we use the inverse of the binary orbital frequency (Ω_{bin}) as a characteristic timescale, the binary mass (M) as a characteristic mass scale, and the semi-major axis of the binary's orbit (a) as a characteristic length scale. All of our results from this study have been reported using this framework. It is, however, useful to convert these results into more physical values. Because our results are applicable to a wide range of binary masses, we choose to scale the binary to a solar mass ($M' \equiv \frac{M_{bin}}{M_\odot}$). We scale the binary's semi-major axis to 0.1 parsecs ($a' = \frac{\text{s.m. axis}}{0.1\text{pc}}$). Finally, we introduce the unitless factor ($\gamma = \frac{\Sigma_0 a^2}{M}$) which relates the unitary disk surface density to the binary mass. Using these definitions, we get a characteristic timescale of $\Omega_{bin}^{-1} = 0.48$ Myr $(M')^{1/2}$ $(a')^{3/2}$. In Table 5.1 we show our results recast in these units. The accretion rate of a $q = 1$ binary accreting at the Eddington limit is 0.022 Myr^{-1} for a radiative efficiency $\eta = 0.1$ (Schnittman & Krolik, 2015). This is the inverse of the Salpeter time. To further elucidate our findings, we display our accretion rate results as a fraction of this fiducial accretion rate. We also display the the accretion timescale $\frac{M}{\dot{M}}$ for each disk.

In reality γ should be $\ll 1$. To estimate a value for γ, we write $\dot{M} = \dot{M}_{sim}$ $(\Sigma_0\, a^2\, \Omega_{bin})$ as a constant times the fiducial Eddington accretion rate ($\dot{M} = \zeta\, \dot{M}_{Edd}$). This allows us to write $\gamma = \frac{\zeta}{\dot{M}_{sim}} \frac{t_{\text{orbit}}}{t_{\text{Salpeter}}}$. We define $M_8 \equiv \frac{M_{bin}}{1E8\, M_\odot}$, and assume a value of $\dot{M}_{sim} \sim 0.03$. This yields a value of $\gamma \sim 3.5\text{E-}5\, \zeta\, (M_8)^{1/2}\, (a')^{3/2}$.

	e = 0.2	**e = 0.4**	**e = 0.6**	**e = 0.8**
$\frac{\dot{M}}{\dot{M}_{Edd}}$	1.8	2.7	4.5	5.0
$\frac{\dot{M}}{M}$	25	16	10	9.1
$\frac{\dot{e}}{e}$	-1.2 ± 0.1	-0.84 ± 0.3	-0.71 ± -0.2	-0.46 ± 0.08
$\frac{\dot{a}}{a}$	-0.6 ± 0.06			

Table 5.1: Our simulation results recast in physical units. The accretion rate ratios are unitless, but have scaling factors: $[\gamma\ (M')^{3/2}\ (a')^{-5/2}]$. The accretion timescales have units [Myr γ^{-1} $(M')^{1/2}$ $(a')^{3/2}$]. The eccentricity and semi-major axis evolution rates have units [Myr^{-1} $\gamma\ (M')^{-1/2}$ $(a')^{-3/2}$].

Future work must include the binary onto the computational grid. This will allow us to better track the disk material as it accretes onto the binaries. By better understanding the manner in which the disk matter impacts the binary members, we will be able to develop a stronger model of the time evolution of the binary's orbital energy and thus the evolution of its orbital characteristics.

Bibliography

Armitage, P. J., & Natarajan, P. 2002, ApJL, 567, L9

Artymowicz, P., & Lubow, S. H. 1994, ApJ, 421, 651

—. 1996, ApJL, 467, L77

Balbus, S. A., & Hawley, J. F. 1991, ApJ, 376, 214

—. 1998, RvMP, 70, 1

Bankert, J., Krolik, J., & Shi, J.-M. 2015, ApJ, 801, 114

Begelman, M. C., Blandford, R. D., & Rees, M. J. 1980, Nature, 287, 307

Blaes, O. M., & Balbus, S. A. 1994, ApJ, 421, 163

Cuadra, J., Armitage, P. J., Alexander, R. D., & Begelman, M. C. 2009, MNRAS, 393, 1423

Dotti, M., Ruszkowski, M., Paredi, L., et al. 2009, MNRAS, 396, 1640

Escala, A., Larson, R. B., Coppi, P. S., & Mardones, D. 2004, ApJ, 607, 765

—. 2005, ApJ, 630, 152

Farris, B. D., Duffell, P., MacFadyen, A. I., & Haiman, Z. 2014, ApJ, 783, 134

Goicovic, F. G., Sesana, A., Cuadra, J., & Stasyszyn, F. 2016, arXiv, arXiv:1602.01966

Goldreich, P., & Tremaine, S. 1980, ApJ, 241, 425

Gould, A., & Rix, H.-W. 2000, ApJL, 532, L29

Hawley, J. F., Guan, X., & Krolik, J. H. 2011, ApJ, 738, 84

Krumholz, M. R., Klein, R., Mckee, C., Offner, S., & Cunningham, A. 2009, Science, 323, 754

MacFadyen, A. I., & Milosavljević, M. 2008, ApJ, 672, 83

Martin, R., Lubow, S., Nixon, C., & Armitage, P. 2016, MNRAS, 458, 4345

Mayer, L., Kazantzidis, S., Madau, P., et al. 2007, Science, 316, 1874

Merritt, D., & Poon, M. Y. 2004, ApJ, 606, 788

Meyer-Vernet, N., & Sicardy, B. 1987, Icarus, 69, 157

Miller, M. C., & Krolik, J. H. 2013, ApJ, 774, 43

Milosavljević, M., & Merritt, D. 2001, ApJ, 563, 34

—. 2003, ApJ, 596, 860

Milosavljević, M., & Phinney, E. S. 2005, ApJ, 622, L93

Miranda, R., Munoz, D., & Lai, D. 2016, MNRAS, 466, 1170

Nixon, C. J. 2012, MNRAS, 423, 2597

Nixon, C. J., Cossins, P. J., King, A. R., & Pringle, J. E. 2011a, MNRAS, 412, 1591

Nixon, C. J., King, A. R., & Pringle, J. E. 2011b, MNRAS, 417, L66

Nixon, C. J., & Lubow, S. H. 2015, MNRAS, 448, 3472

Noble, S. C., Krolik, J. H., & Hawley, J. F. 2010, ApJ, 711, 959

Noble, S. C., Mundim, B. C., Nakano, H., et al. 2012, ApJ, 755, 51

Paczyński, B. 1977, ApJ, 216, 822

Papaloizou, J., & Lin, D. N. C. 1984, ApJ, 285, 818

Papaloizou, J., & Pringle, J. E. 1977, MNRAS, 181, 441

Pringle, J. E. 1991, MNRAS, 248, 754

Rafikov, C. 2016, ApJ, 827, 12

Roedig, C., Krolik, J., & Miller, C. 2014, ApJ, 785, 115

Roedig, C., & Sesana, A. 2014, MNRAS, 439, 3476

Roedig, C., Sesana, A., Dotti, M., et al. 2012, ApJ, 545, 13

Sano, T., Inutsuka, S.-i., Turner, N. J., & Stone, J. M. 2004, ApJ, 605, 321

Schnittman, J., & Krolik, J. 2015, ApJ, 806, doi:10.1088/0004-637X/806/1/88

Shakura, N. I., & Sunyaev, R. A. 1973, A&A, 24, 337

Shi, J.-M., & Krolik, J. H. 2015, ApJ, 807, 12

Shi, J.-M., Krolik, J. H., Lubow, S. H., & Hawley, J. F. 2012, ApJ, 749, 118

Sorathia, K. A., Krolik, J. H., & Hawley, J. F. 2015, ApJ, 777, doi:10.1088/0004-637X/777/1/21

Sorathia, K. A., Reynolds, C. S., Stone, J. M., & Beckwith, K. 2012, ApJ, 749, doi:10.1088/0004-637X/749/2/189

Stone, J. M., & Norman, M. L. 1992a, ApJS, 80, 753

—. 1992b, ApJS, 80, 791

Tang, Y., MacFadyen, A., & Haimann, Z. 2017, ArXiv e-prints, arXiv:1703.03913

Vasiliev, E., Antonini, F., & Merritt, D. 2013, ArXiv e-prints, arXiv:1311.1167

—. 2015, ApJ, 810, doi:10.1088/0004-637X/810/1/49

Volonteri, M., Haardt, F., & Madau, P. 2003, ApJ, 582, 559

Curriculum Vitae

Justin Bankert was born in Indianapolis, Indiana on September 29, 1987. He was the first in his family to attend college. He graduated from Purdue University with a bachelor's degree in math and a bachelor's degree in physics while minoring in astronomy. As an undergraduate student he worked as a teaching assistant and as a research assistant. His undergraduate research focused on (1) catalogues of galaxy clusters and (2) work with the LSST image simulation team preparing images to test the automation of the LSST analysis algorithms. He was accepted to the Johns Hopkins Department of Physics and Astronomy for graduate school. There he again worked as both a teaching assistant and research assistant. His graduate research focused on circumbinary accretion disk physics. In 2012, he attained a Masters degree in physics from Johns Hopkins University. In 2016, he completed the Preparing Future Faculty program in the Johns Hopkins Teaching Academy. On August 11, 2017 he defended his doctoral thesis before going to Angelo State University for a one year Visiting Assistant Professor position.